AGU PUBLICATIONS

Geochemistry, Geophysics, Geosystems

RESEARCH ARTICLE
10.1002/2014GC005684

Gravity anomalies, crustal structure, and seismicity at subduction zones: 1. Seafloor roughness and subducting relief

Dan Bassett[1,2] and Anthony B. Watts[1]

[1]Department of Earth Sciences, University of Oxford, South Parks Road, Oxford, UK, [2]Now at Scripps Institution of Oceanography, La Jolla, California, USA

Companion to *Bassett and Watts* [2015], doi:10.1002/2014GC005685.

Key Points:
- A new method of isolating short wavelength structure in fore arcs is developed
- >200 bathymetric anomalies are related to the structure of the subducting plate
- The expression of subducting relief is largest where upper plate rigidity is low

Supporting Information:
- Supporting Information S1
- Supporting Information S2
- Supporting Information S3

Correspondence to:
D. Bassett,
dbassett@ucsd.edu

Citation:
Bassett, D., and A. B. Watts (2015), Gravity anomalies, crustal structure, and seismicity at subduction zones: 1. Seafloor roughness and subducting relief, *Geochem. Geophys. Geosyst.*, *16*, doi:10.1002/2014GC005684.

Received 8 DEC 2014
Accepted 5 MAR 2015
Accepted article online 14 MAR 2015

Abstract An ensemble averaging technique is used to remove the long-wavelength topography and gravity field from subduction zones. >200 residual bathymetric and gravimetric anomalies are interpreted within fore arcs, many of which are attributed to the tectonic structure of the subducting plate. The residual-gravimetric expression of subducting fracture zones extends >200 km landward of the trench axis. The bathymetric expression of subducting seamounts with height ≥1 km and area ≥500 km^2 (N=36), and aseismic ridges (N>10), is largest near the trench (within 70 km) and above shallow subducting slab depths (SLAB1.0 <17 km). Subducting seamounts are similar in wavelength, amplitude, and morphology to unsubducted seamounts. Morphology, spatial distributions, and reduced levels of seismicity are considered inconsistent with mechanical models proposing wholesale decapitation, and the association of subducting seamounts with large-earthquakes. Subducting aseismic ridges are associated with uplift and steepening of the outer fore arc, a gradual reduction in residual bathymetric expression across the inner fore arc, and a local increase in the width and elevation of the volcanic-arc/orogen. These contrasting expressions reflect the influence of margin-normal variations in rigidity on where and how the upper plate deforms, both to accommodate subducting relief and in response to stresses transmitted across the plate interface. The outer fore arc and arc have lower rigidity due to fracturing and thermal weakening, respectively. Similar associations with complex earthquakes and fault creep suggest aseismic ridge subduction may also be accommodated by the development and evolution of a broad fracture network, the geometrical strength of which may exceed the locking strength of a smooth fault.

1. Introduction

The association of subducting seafloor roughness with seismic gaps and the segmentation of subduction megathrusts was originally made in the 1970s [*Sykes*, 1971; *Kelleher et al*., 1973, 1974; *Kelleher and McCann*, 1976; *Spence*, 1977], has been recently reviewed by *Wang and Bilek* [2014], and remains a subject of debate. Despite a widely held expectation that subducting topographic features should result in strong coupling and large earthquakes [*Cloos*, 1992; *Scholz and Small*, 1997; *Kumagai et al*., 2012]; most observations show seamounts [*Kodaira et al*., 2002; *Mochizuki et al*., 2008], aseismic ridges [*Spence et al*., 1999; *Bilek*, 2010; *Sparkes et al*., 2010], and fracture zones [*Spence*, 1977; *Schöffel and Das*, 1999; *Robinson et al*., 2006] impeding or terminating seismic rupture, and geodetic observations suggest creeping is the predominant mode of subduction in regions of rough seafloor [*Wang and Bilek*, 2014]. As demonstrated by the 2007 Mw 8.1 Solomon Islands earthquake [*Taylor et al*., 2008], there are exceptions where large earthquakes [*Protti et al*., 1995; *Abercrombie et al*., 2001; *Bilek et al*., 2003; *Bilek and Engdahl*, 2007; *Robinson and Cheung*, 2010] and strong coupling [*Wallace et al*., 2012] has been associated with subducting topographic relief, but regional or global syntheses generally show a negative correlation between large earthquakes (Mw ≥ 8) and rough seafloor [*Kelleher and McCann*, 1976; *Morgan et al*., 2008; *Sparkes et al*., 2010; *Kopp*, 2013], or the equivalent positive correlation between large earthquakes and seafloor smoothed by thick sediment volumes [*Ruff*, 1989; *Scholl et al*., 2011; *Heuret et al*., 2012].

The main objective of this study is to place new regional constraints on where subducting topographic features are likely present within seismogenic zones, which is important under either seismotectonic scenario for improving understanding of how bathymetric features subduct and evaluating seismic hazard.

Along strike, there are over 50,000 km of subduction fore arcs on Earth [*Bird*, 2003]. Most seismogenic zones lie underwater making them challenging and expensive regions to study, while

compounding the dangers of ground shaking with associated tsunami. Most regional studies are thus conducted by directly comparing seafloor structure seaward of the trench axis with seismological and/or geodetic inferences of megathrust slip behavior on the landward side [*Sparkes et al*., 2010; *Wang and Bilek*, 2014]. Many structures such as hot-spot generated seamounts, aseismic ridges, and fracture zones on the subducting oceanic plate are sufficiently linear that approximate locations within the seismogenic zone can be estimated from their geometry seaward of the trench axis [*Robinson et al*., 2006; *Sparkes et al*., 2010]. But the majority of seamounts are not organized in linear chains [*Hillier and Watts*, 2007] and assumptions of geometrical continuity across the trench axis are not always valid [*Bassett*, 2014]. Gravity-derived models are of limited use, particularly where unconstrained by seismic data. Magnetic models are also limited, but have been used to discriminate between fore-arc seamounts associated with serpentinite diapirism, having little or no magnetic signature (e.g., Mariana: [*Hussong and Uyeda*, 1982]), and those associated with positive magnetic anomalies and subducting seamounts in Costa Rica [*Barckhausen et al*., 1998], Cascadia [*Tréhu et al*., 2012], and Hikurangi [*Bell et al*., 2010]. Direct observations of subducting relief come from seismic reflection [*Ranero and von Huene*, 2000; *Bangs et al*., 2006; *Barker et al*., 2009; *Bell et al*., 2010; *Singh et al*., 2011] and refraction [*Kodaira et al*., 2000; *Kodaira et al*., 2002; *Mochizuki et al*., 2008] surveys, but these data are relatively sparse and unevenly distributed. Global grids of bathymetry [*IOC*, 2003] and free-air gravity anomalies [*Sandwell and Smith*, 2009; *Sandwell et al*., 2014] are the only data sets uniform in resolution across all subduction zones, but it is often difficult to identify short-wavelength structure within the high gravimetric and topographic gradients that characterize fore arcs. Earlier studies have attempted to remove these gradients by calculating trench-parallel gravity [*Song and Simons*, 2003] and bathymetric [*Bassett*, 2014] anomalies, and both *Wells et al*. [2003] and *Song and Simons* [2003] posit relationships between the seismic asperities of great earthquakes with free-air and trench-parallel gravity anomalies, respectively.

In this study, we extend spectral averaging techniques developed to isolate residual bathymetric anomalies associated with Louisville Ridge seamounts subducting beneath the Tonga-Kermadec fore arc [*Bassett*, 2014] to all subduction zones on Earth. We present these results in two parts. Part 1 (this manuscript) is focused on subducting plate structure and new spatial constraints on the distribution of subducting bathymetric features allow relations with slip behavior and mechanical models of relief subduction to be reconsidered. Part 2 [*Bassett and Watts*, 2015] is focused on interrelationships between overthrusting plate structure with slip-behavior and describes observations relating trench-parallel fore-arc ridges to the dimensions of seismogenic zones. This study is global in focus and the grids developed for each margin are made available as an electronic supplement and online for future use.

2. Methodology

2.1. Construction of Residual Free-Air Gravity and Topography Grids

Gravity and topography data place important constraints on both shallow and deep crustal structure and are central to our understanding of the isostatic, nonisostatic (i.e., dynamic) and tectonic processes that sculpt Earth's crust and mantle (Figure 1). In this study we analyze the 1 × 1 min satellite-derived free-air gravity anomaly grid [*Sandwell et al*., 2014] and the GEBCO 1 × 1 min shipboard bathymetry grid (Version 2.0) [*IOC*, 2003]. The 1 × 1 min GEBCO grid does not incorporate satellite-derived bathymetry data and land elevations are integrated from the Global Land One-km Base Elevation (GLOBE) project data set [*Hastings and Dunbar*, 1998]. Free-air gravity anomalies offshore are calculated from radar altimeter measurements of ocean-surface heights and are merged with subaerial gravity anomalies from the EGM2008 global gravity model [*Sandwell and Smith*, 2009; *Pavlis et al*., 2012]. The recent addition of nonrepeat data from the CryoSat-2 and Jason-1 altimeters has improved accuracy offshore by a factor of 2–4 and the most recent gravity grid (Version 23.1) has a precision of ~2 mGal [*Sandwell et al*., 2014].

Across subduction zones, the free-air gravity anomaly and topography fields are dominated by a long-wavelength high and low associated with the island-arc or orogen and the deep-sea trench, respectively (Figure 1). The large amplitude of these highs (up to 4 km and 200 mGal relative to the back arc) and lows (up to −4 km and −350 mGal relative to the abyssal plain) are well known from early submarine and shipboard measurements [*Vening-Meinesz et al*., 1932; *Talwani et al*., 1959; *Talwani et al*., 1961; *Worzel*, 1965;

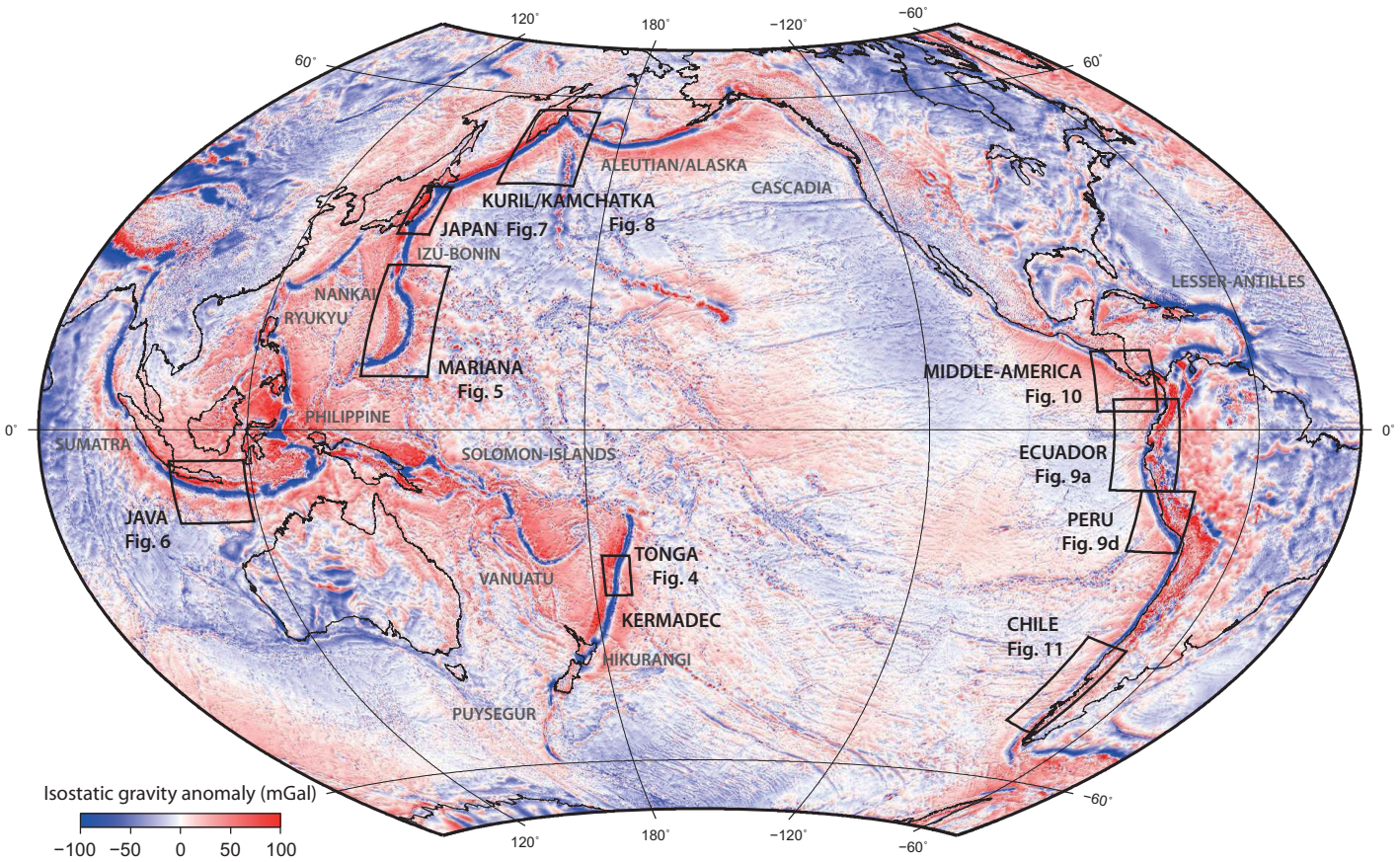

Figure 1. Airy-Heiskanen isostatic gravity anomalies ($T_c = 37.5$ km $\rho_w = 1030$ kg/m^3, $\rho_c = 2670$ kg/m^3, $\rho_w = 3330$ kg/m^3) of the circum-Pacific ocean basin showing figure locations.

Hayes, 1966; *Hayes and Ewing*, 1970; *Watts and Talwani*, 1974; *Watts and Talwani*, 1975] and are similarly present and well resolved by satellite-derived solutions and altimetry [*Sandwell and Smith*, 1997; *Smith and Sandwell*, 1997; *Sandwell et al*., 2014].

The fore-arc region of subduction zones separates the peaks of these paired anomalies and is thus characterized by high topographic (mean ∼3.5°) and gravimetric (mean ∼2 mGal km^{-1}) gradients. These gradients can overwhelm lower-amplitude shorter-wavelength signals, thereby masking considerable detail in the structure of the fore arc, arc, and back arc. The objective of this paper is to isolate and remove the average trench-normal profile. This procedure reduces the trench-normal dynamic range, removes the steep gradients associated with the seaward and landward trench-slopes, and significantly increases the resolvability of short-wavelength lower-amplitude structure.

The process by which this is achieved is illustrated in Figure 2. For each subduction margin, the average trench-normal profile is calculated by sampling regional grids of bathymetry and free-air gravity anomaly along trench-perpendicular profiles extending >600 km up and downdip of trench axis and spaced ∼25 km along strike. The trench axis is defined as the deepest point using the GEBCO08 bathymetric grid [*IOC*, 2003]. A Fast-Fourier-Transform is used to calculate the frequency spectrum of each profile. The average frequency spectrum is then calculated from the Fourier coefficients at each frequency before an inverse transform is applied to calculate the ensemble average trench-normal profile for each data set and margin. The linearity of the Fourier transform and its inverse means spectral averages should be identical to arithmetic or stacked averages, however, small differences resulting from finite precision of the Fourier transform and associated downsampling are present for small ensembles (< 30 profiles) (supporting information Figure 1). Maintaining the geometry of the trench, grids of each average profile are created and subtracted from the original data sets to produce grids of residual bathymetry and residual free-air gravity anomaly. As opposed to methodologies involving regridding of residuals calculated along profiles, the subtraction of an

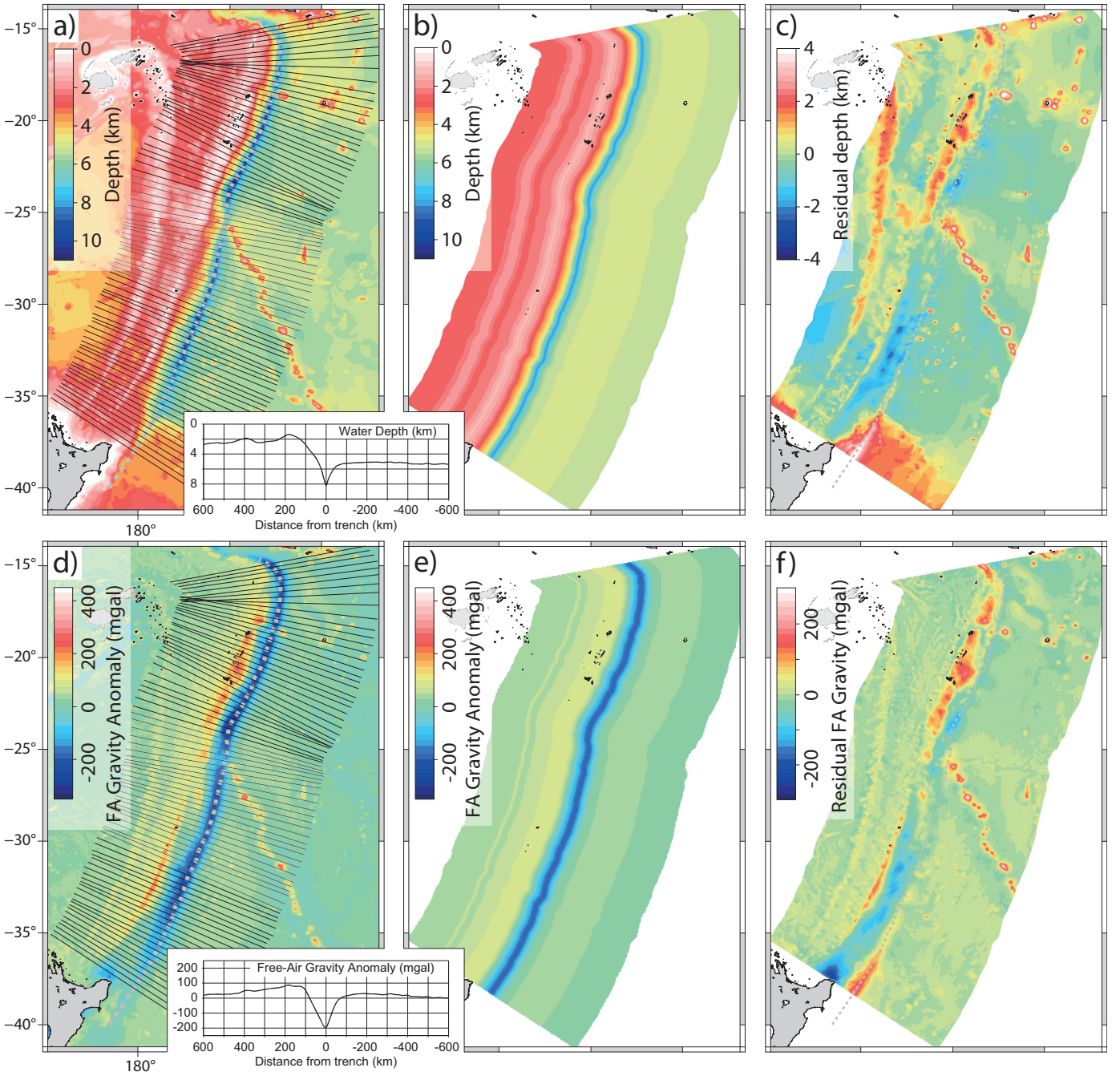

Figure 2. Figures illustrating the ensemble averaging and grid processing methodology as applied at the Tonga-Kermadec subduction zone. Regional grids of (a–c) bathymetry [*IOC*, 2003] and (d–f) free-air gravity anomaly [*Sandwell et al.*, 2014] are sampled along trench-normal profiles (a and d). The spectral average is calculated from each ensemble of profiles (b and e inset). Maintaining the geometry of the trench, grids of the average profile are constructed (b and e), and subtracted from the original data sets to reveal (c) residual bathymetry and (f) residual free-air gravity anomaly.

ensemble average grid preserves the full (1 × 1 min) resolution of the original data sets (supporting information Figure 2).

Ensemble average profiles of the Airy-Heiskanen isostatic gravity anomaly are also calculated for each margin and are dashed in gray in Figure 3b. There is a close agreement between the ensemble free-air and isostatic gravity anomalies and so the long-wavelength component of both anomaly data sets inform us of the nonisostatic, dynamic, contribution to Earth's gravity field in subduction zones.

2.2. Seismicity

Structural observations from residual gravity and topography anomalies are compared with seismological and geodetic inferences of megathrust slip-behavior. Many of the regions considered in this study (Figure 1) are characterized by a lack of large magnitude (Mw$\geq$8) earthquakes and the Global Centroid Moment Tensor (GCMT) [*Dziewonski et al*., 1981; *Ekström et al*., 2012], Engdahl, van der Hilst, and Buland (EHB) [*Engdahl et al*., 1998], and International Seismological Center (ISC) (http://www.isc.ac.uk/ accessed January 2015) earthquake bulletins are integrated with geodetic inferences of plate boundary locking. A large magnitude earthquake catalog compiled for this study containing the epicenters, seismic asperities, and slip distributions for over 150 of the largest (Mw 7–9.5) subduction zone earthquakes is presented and analyzed in part 2 [*Bassett and Watts*, 2015].

We are interested here in earthquakes occurring on the megathrust and extract events of all magnitudes from the GCMT catalog (period 1976 to July 2013) with thrust faulting mechanisms (T-axis plunge $\geq 45^\circ$, P-axis plunge $\leq 45^\circ$), centroid depth $\leq$ 65 km [*Heuret et al*., 2011; *Hayes et al*., 2012], and with strike and dip within 20° and 15°, respectively, of the subducting SLAB1.0 geometry [*Hayes et al*., 2012]. The full duration (1960–2009) and magnitude range (mb $\geq$ 3) of the EHB catalog is downloaded and reported event times are used to relocate GCMT centroids to their EHB hypocenters. Unless stated otherwise, earthquake density is calculated as the number of events with depth $\leq$ 65 km within a 10 km search radius using the EHB catalog for the period 1960–2009 and the reviewed ISC catalog (Mw $\geq$3.0) for the period 2010–2012.

3. Global Ensemble Average Profiles

Ensemble average profiles calculated for topography, free-air gravity anomaly, and Airy-Heiskanen isostatic gravity anomaly (dashed) for each margin are displayed in Figure 3. We also display the global ensemble average profile that is calculated from, and shown overlying, the stack of average profiles for each margin segment normalized across distances 300–600 km seaward of the trench axis (Figure 3) [*Hatherton*, 1969; *Hayes and Ewing*, 1970].

Seaward of the trench, ensemble profiles reveal a several hundred kilometer wide belt of free-air gravity anomalies of +50–60 mGal that mark the Outer Gravity High [*Watts and Talwani*, 1974]. This gravity anomaly is accompanied by a regional rise in topography of several hundred meters. The Outer Gravity High and steep gravity gradient associated with the seaward wall of the trench are almost entirely fit by the computed gravity effect of topography assuming a water/mantle density contrast of 2270 kg m^3 [*Watts and Talwani*, 1975]; and have been modeled as the flexure of an elastic plate [*Hanks*, 1971; *Watts and Talwani*, 1975; *Parsons and Molnar*, 1976; *McAdoo et al*., 1978; *Bodine and Watts*, 1979; *Levitt and Sandwell*, 1995; *Bry and White*, 2007]. Flexure is modulated by the effective elastic thickness (T_e) of the subducting lithosphere, which new analysis suggests is strongly linked with its age [*Hunter et al*., 2013].

The negative free-air gravity anomaly in the vicinity of the trench, a significant part of which cannot be explained by isostatic models, is not always coincident with the trench axis and is sometimes displaced over the landward trench slope due to displacement of crustal materials by low-density sediments. Analogous to the seaward trench slope, the gravity gradient landward of the trench primarily reflects the topography of the fore arc; however, the controls on this gradient are more complex. Elastic plate theory [*Davies*, 1981], shearing of a viscous accretionary wedge [*Emerman and Turcotte*, 1983], and cohesive Coulomb wedge theory [*Davis et al*., 1983; *Dahlen*, 1984; *Dahlen et al*., 1984; *Dahlen*, 1990; *Wang and Hu*, 2006] have all been proposed to explain the geometry of the landward trench slope. Viscous-flow models show downwarping of the overriding plate as a direct consequence of dynamic coupling to the negative buoyancy force of the subducting slab through the wedge [*Zhong and Gurnis*, 1992, 1994]. This slab induced downwarping, however, is broad (>400 km), centered landward of the trench approximately above the slab center of mass [*Hager*, 1984], and is quite different from observed topography. The inclusion of a low-viscosity wedge in dynamic flow models reduces coupling through the wedge [*Billen and Gurnis*, 2001, 2003; *Billen et al*., 2003] and inclusion of the plate boundary as a fault in viscous flow models is necessary to reproduce the short-wavelength, high-amplitude near-trench topography [*Zhong and Gurnis*, 1992; *Zhong et al*., 1998]. The gravity effect of the subducting slab beneath the fore arc is small, either because the density contrast is small or because the slab is regionally compensated at depth [*Watts and Talwani*, 1975; *Davies*, 1981].

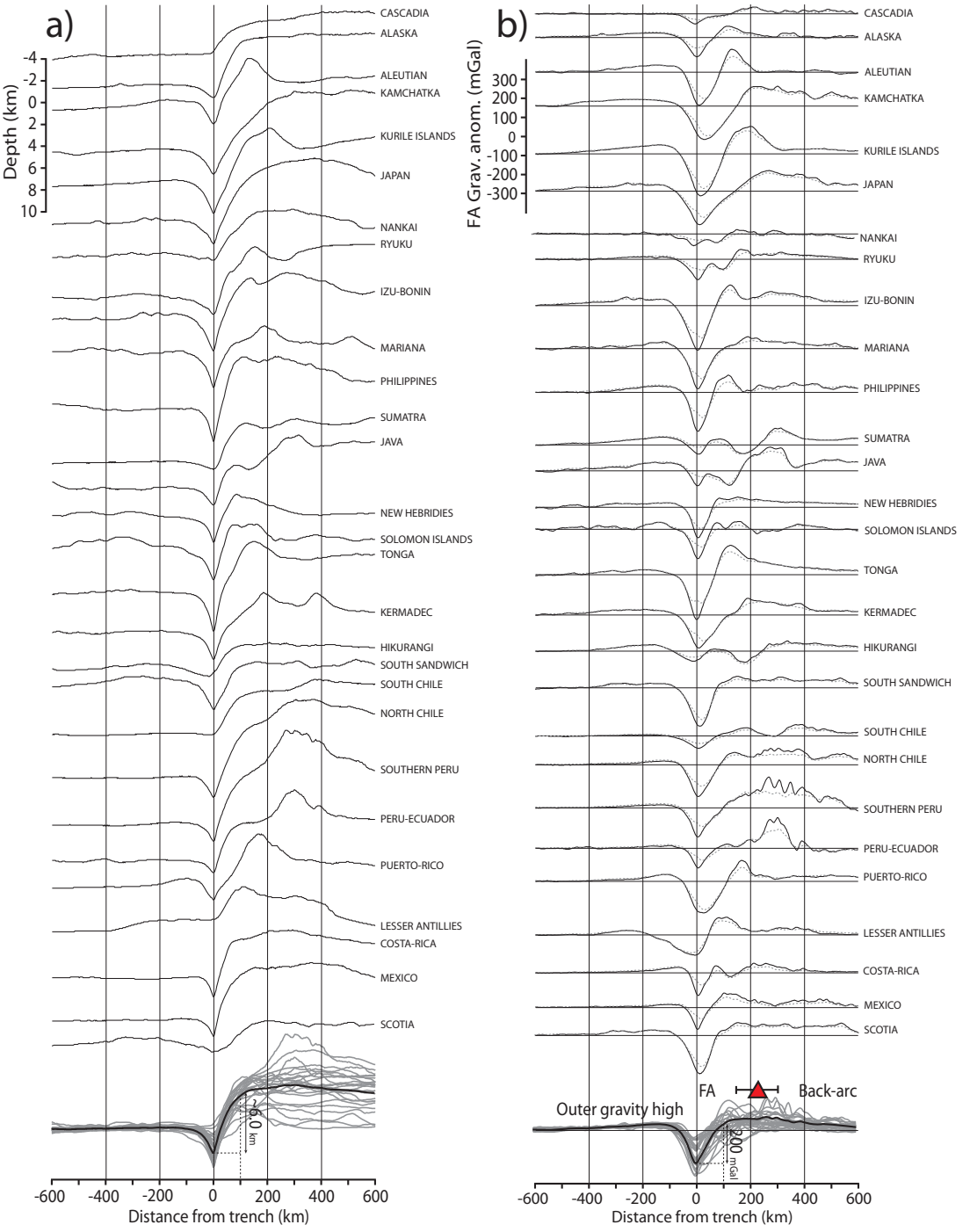

Figure 3. Ensemble average profiles of (a) topography and (b) free-air gravity anomaly stacked on the trench axis. Dashed profiles in Figure 3b show the average Airy-Heiskanen isostatic gravity anomaly. For each data set, average profiles of each margin are normalized 300–600 km seaward of the trench axis and stacked at the bottom of each plot. The global average of these profiles is shown in black. FA = Fore arc. Red triangle with bars marks the location of most volcanic arcs [*Syracuse and Abers*, 2006].

Landward of the fore arc, the ensemble profile shows a broad free-air gravity high that decreases by ~50 mGal across the back arc (Figure 3b). This shallow gradient is flanked in some, predominantly oceanic-oceanic, margins by a narrower (100–200 km), large amplitude (>100 mGal) high coincident with the island arc. These gravity anomalies reflect the combined effects of the topography and compensation of the island arc, and the dynamics of the back arc.

The close correspondence between the ensemble average profiles calculated from isostatic and free-air gravity anomalies (Figure 3b) suggests that the residual gravity-anomaly does indeed represent the non-isostatic contribution to the trench-normal gravity signal. At short-wavelengths, the residual probably reflects the fore-arc, arc, and back-arc structure while at long-wavelengths it probably reflects dynamic processes such as those associated with sinking slabs and flow in the overlying mantle wedge.

4. Interpretations of Subducting Relief

The seafloor is far from uniform and comprises a rich mosaic of volcanic and tectonic structures including seamounts [*Hillier and Watts*, 2007], large igneous provinces [*Coffin and Eldholm*, 1994], fracture zones, and aseismic, active and extinct ocean ridges [*Matthews et al*., 2011]. When carried into subduction zones, these structures have been shown to modulate seismogenic processes [*Kelleher and McCann*, 1976; *Bilek et al*., 2003; *Robinson et al*., 2006; *Mochizuki et al*., 2008; *Das and Watts*, 2009; *Sparkes et al*., 2010] and the morphology, subsidence, and uplift history of the fore arc [*Lallemand and Le Pichon*, 1987; *Lallemand et al*., 1989; *Dominguez et al*., 1998; *Dominguez et al*., 2000; *Oakley et al*., 2008]. The morphological imprint on the fore arc is well expressed in grids of residual bathymetry and residual free-air gravity anomaly. In this section, these observations are presented alongside the relations shown with seismicity.

5. Seamounts

5.1. The Louisville Ridge Seamount Chain: Tonga Trench Collision Zone

At $\sim$26°S, the Tonga trench is intersected by the Louisville Ridge seamount chain [*Hayes and Ewing*, 1971; *Lonsdale*, 1986; *Watts et al*., 1988; *Ballance et al*., 1989; *Koppers et al*., 2004, 2012]. West of Osbourn, which is the oldest unsubducted seamount, the residual bathymetric grid shown in Figure 4a reveals a 70–80 km wide belt of positive bathymetric anomalies $>$1 km in amplitude extending 60 km across the fore arc.

Occupying the trench, the largest anomaly is associated with Mo'unga seamount, which was previously recognized as a conical, 1.5 km high, and 10 km wide uplift from swath bathymetry data [*Lonsdale*, 1986; *Pontoise et al*., 1986; *Ballance et al*., 1989; *Stratford et al*., 2015]. The residual bathymetric grid suggests a NE-SW elliptical geometry for Mo'unga with amplitude $>$2.5 km and semi-major and semi-minor axes of $\sim$50 and $\sim$25 km, respectively. A second smaller residual bathymetric high (amplitude $>$1.5 km) is observed NW of Mo'unga. Both highs are located up to $\sim$50 km south of the projected track of the unsubducted Louisville Ridge, along which bathymetric anomalies are typically $\leq$1 km in amplitude.

The Louisville collision zone has been the subject of two recent marine-geophysical research cruises [*Grevemeyer and Flueh*, 2008; *Peirce and Watts*, 2011] and seismic reflection and refraction data calibrate the association of residual bathymetric anomalies with subducting relief. Figure 4c shows two preliminary forward P-wave velocity (V_P) models from *Bassett* [2014].

Section A-A' is dip parallel, traverses both Osbourn and Mo'unga, and shows both seamounts to be associated with a 2–3 km increase in thickness of a layer overlying the subducting Pacific plate crust with V_P 4.2–5.3 km s^{-1}. A third increase in layer thickness is modeled at greater depth, beneath the smaller residual bathymetric high, but this model region is not well constrained.

Section G-G' is strike-parallel and traverses this smaller high, which is correlated with peaks in free-air gravity (+60 mGal) and magnetic (+280 nT) anomalies. This profile reveals a sharp and local reduction in fore-arc velocity gradient, with seismic wave speeds between 2 and 12 km depth (b.s.f.) $>$1.0 km s^{-1} slower than those observed 20 km north and south of the bathymetric high at equivalent depth. A low-velocity body is modeled above the Pacific plate crust from wide-angle reflections, but wave speeds near the slab–fore-arc-Moho intersection are not well constrained.

Despite alignment with the unsubducted Louisville Ridge, preliminary analysis of refraction data along Profile C resolves no subducting seamounts beneath the fore arc [*Bassett*, 2014]. This velocity-structure is consistent with the absence of both magnetic and residual bathymetric anomalies. A low-velocity

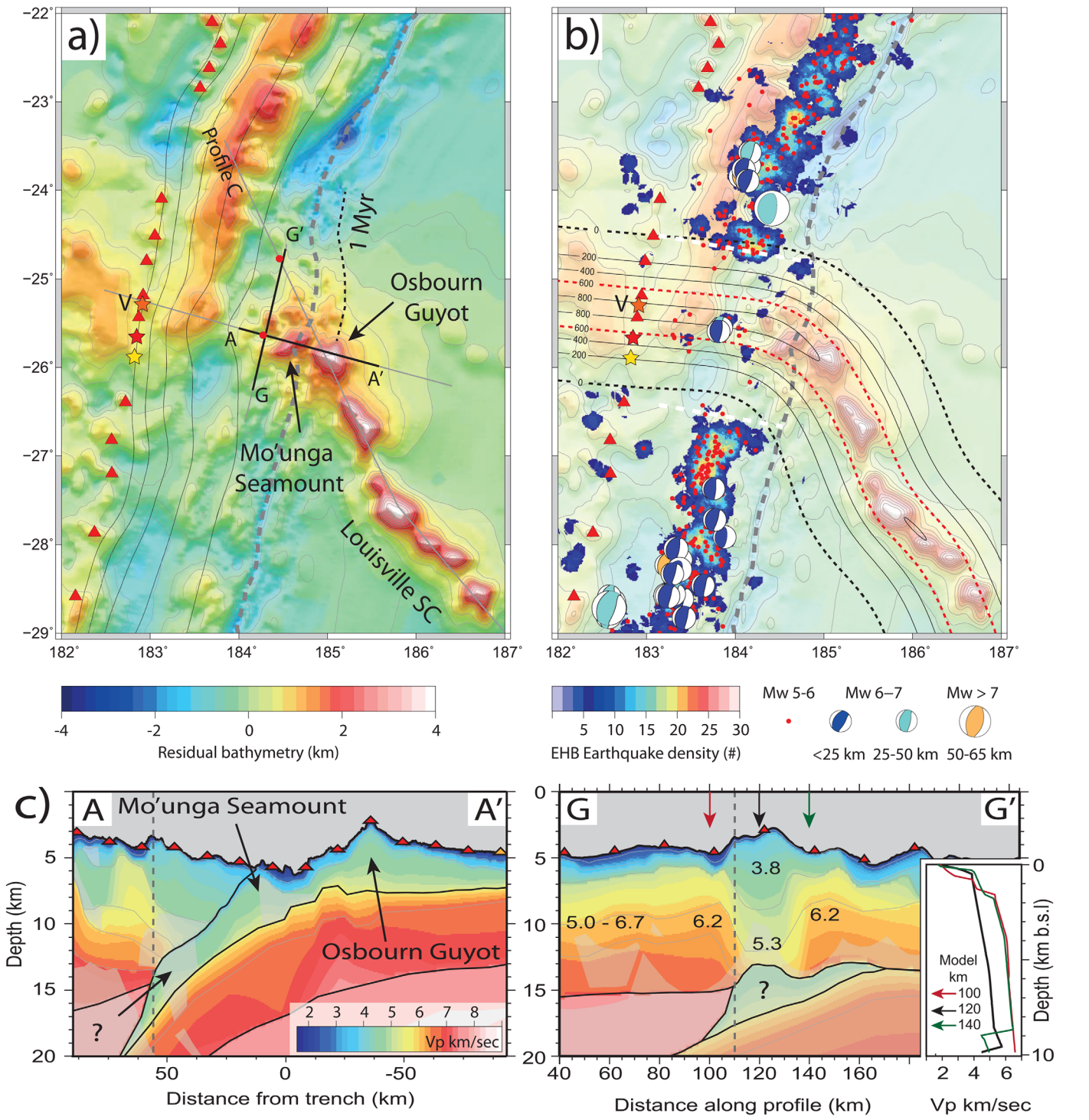

Figure 4. (a) Residual bathymetry in the Louisville Ridge-Tonga trench collision zone. Contours of residual bathymetry (500 m) and subducting SLAB1.0 depth (20 km) are shown in fine gray and black, respectively [*Hayes et al*., 2012]. The trench axis is dashed in gray. Black dash north of the contemporary collision zone marks the possible extent of seamount subduction in the last 1 Myr [*Ballance et al*., 1989]. Note the absence of large bathymetric anomalies within this section of the fore arc. Gray profiles show active source MCS/OBS profiles with the sections displayed in Figure 4c marked in black. Red dots along these profiles mark the subducting slab–fore-arc-Moho intersection. Historically active volcanoes are shown as red triangles [*Simkin and Siebert*, 2002]. Figure 4b EHB/ISC earthquake density and hypocenters for GCMT thrust earthquakes. Contours at 200 m increments show the geometry of the Louisville flexural moat assuming residual bathymetric anomalies in the outer fore arc and the geochemically anomalous arc volcano V [*Timm et al*., 2013] constrain the geometry of the subducting portion of the ridge [*Bassett*, 2014]. Note the correlation between the predicted boundaries of the flexural moat (black dash) with the northern and southern limits of the Louisville seismic gap (white dash). Figure 4c Preliminary forward P-wave (V_P) velocity models of crustal structure along profile segments A-A′ and G-G′ [*Bassett*, 2014]. The velocity model along Profile A-A′ is similar to that published by *Stratford et al*. [2015] and differences are minimal in well-constrained model regions.

(V_P 2.8–5.4 km s^{-1}) layer overlying the Pacific Plate crust to 12 km depth is interpreted as subducting volcaniclastic and pelagic sediments, which accumulate and reach up to 1.5 km thickness in the Louisville Ridge's flexural moat [*Contreras-Reyes et al*., 2010].

These wide-angle seismic models and magnetic anomaly modeling in *Bassett* [2014] support the interpretation of residual bathymetric anomalies as reflecting the presence of subducting bathymetric relief. The subducting slab–fore-arc-Moho intersection is marked by red dots in Figure 4a, and this intersection may spatially limit the expression of subducting bathymetric features in fore-arc morphology.

Morphological characteristics of the Louisville collision zone are accompanied by a sharp 200 km wide reduction in the number of earthquakes known as the "Louisville Gap" [*Habermann et al*., 1986; *Scholz and Small*, 1997]. Earthquake density plotted in Figure 4b shows this gap centered on large residual bathymetric anomalies in the outer fore arc, landward which an isolated cluster of thrust earthquakes give the gap a two-lobbed appearance. This cluster may be analogous to earthquakes observed in-front of subducting seamounts in Japan [*Mochizuki et al*., 2008] and Cascadia [*Tréhu et al*., 2012]. The absence of geodetic observations and the short-duration of instrumental earthquake catalogs make it hard to determine if this gap represents a creeping megathrust, or an interseismically locked seismogenic zone with each lobe capable of generating a future Mw 8.2 earthquake.

The distribution of magnetic and residual bathymetric anomalies may suggest an approximately East-West geometry for the subducting segment of the Louisville Ridge [*Timm et al*., 2013; *Bassett*, 2014]. This geometry is supported by Pb and Sr isotope ratios requiring up to 40% input of Louisville Ridge material into partial melts beneath the arc volcano "V" (Labeled in Figures 4a and 4b); and may also provide one possible physical explanation for the Louisville seismic gap.

The contours in Figure 4b show the geometry of the Louisville flexural moat calculated in 3-D by extending the mean cross-sectional structure of the ridge along the westerly geometry implied by the distribution of residual bathymetric anomalies and using an effective elastic thickness (T_e) of 10 km [*Contreras-Reyes et al*., 2010]. Correlating each lobe of the seismic gap with each flank of the flexural moat, *Bassett* [2014] suggest the locally higher flux of sediment and entrained fluid may reduce the shear strength of the subduction interface. But thicker sediment volumes have also been linked with large earthquakes [*Ruff*, 1989; *Scholl et al*., 2011] and although these scenarios remain hard to distinguish between, seismic-reflection, and morphological observations showing a significantly greater degree of active and pervasive upper plate extensional deformation within the seismic gap lead us to prefer interpretations where the underlying megathrust is weak.

5.2. Mariana Arc

The Mariana arc is commonly regarded as the type example of an erosive, extensional, and aseismic subduction margin [*Uyeda and Kanamori*, 1979; *Hussong and Uyeda*, 1982]. Residual bathymetry is shown in Figure 5b. Three large (diameter $>$50 km, amplitude $\sim$2 km) bathymetric anomalies occupy the central Mariana fore arc and continuity with bathymetric anomalies seaward of the trench axis strongly suggests an association with subducting seamounts. Along the southern Izu-Bonin trench, the subducting Ogasawara Plateau is expressed as a 2–3 km uplift of the outer fore arc, the amplitude and along-strike width ($\sim$180 km) of which is well correlated with plateau dimensions seaward of the trench axis. All observations of subducting relief appear restricted to slab depths $\leq$20 km [*Hayes et al*., 2012], which is similar to 15–20 km crustal thickness estimates from seismic refraction data across the southern Mariana fore arc [*Takahashi et al*., 2007].

Figure 5c shows that earthquake density is largest along the southern Mariana megathrust and a $\sim$600 km long segment has ruptured in $>$70 intermediate magnitude ($5 \leq Mw < 7$) thrust events. No positive residual bathymetric anomalies are observed within this seismic band, the northern termination of which is coincident with a large anomaly likely associated with a subducting seamount. Megathrust seismicity is sparse along the central and northern Mariana arc and all large residual bathymetric anomalies are characterized by low-earthquake density. The amplitudes, form, and relations with seismicity of these anomalies support earlier suggestions that along the Mariana arc, bathymetric relief onboard the Pacific plate may be subducting intact [*Fryer and Smoot*, 1985] and aseismically [*Wang and Bilek*, 2014].

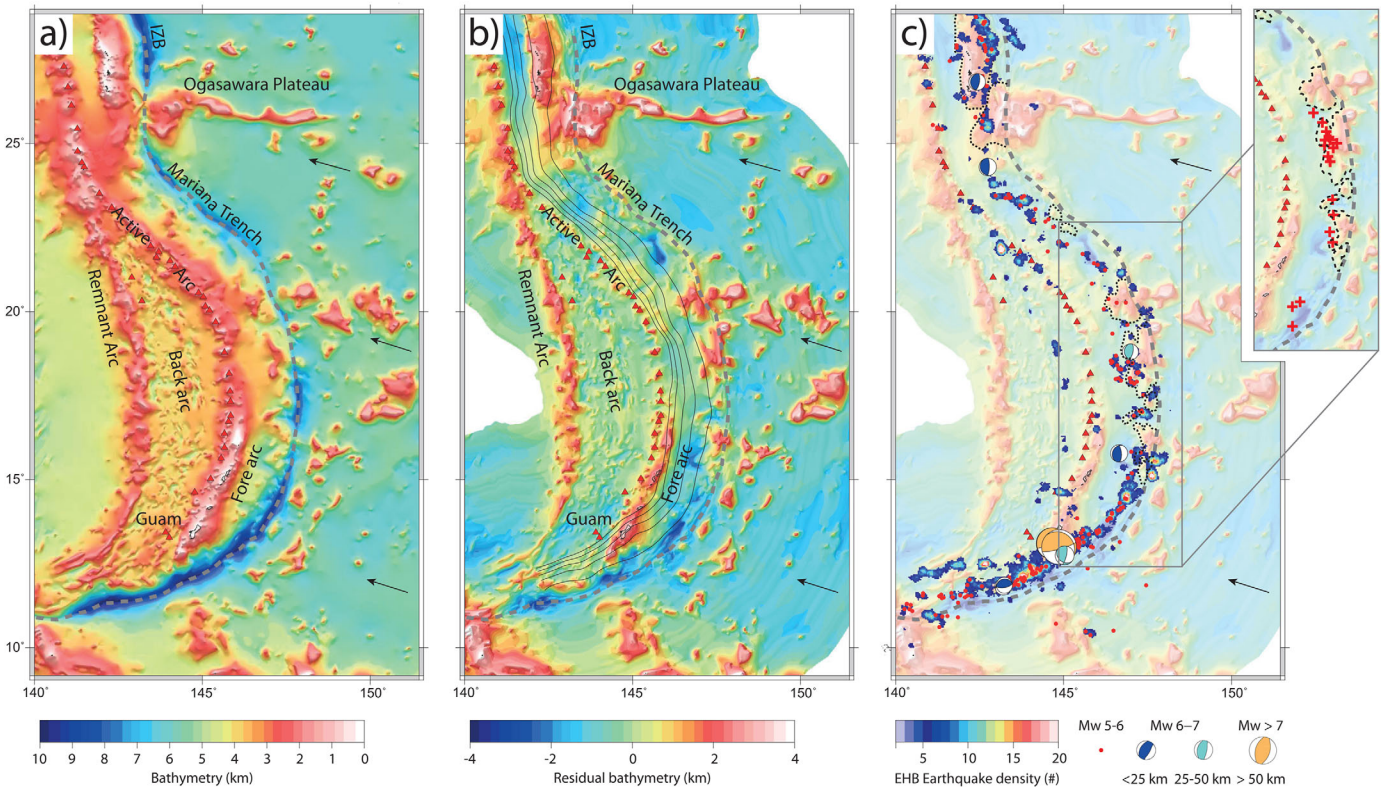

Figure 5. (a) Bathymetry and (b) residual bathymetry for the Mariana subduction zone. Figure nomenclature as in Figure 4. (c) EHB/ISC earthquake density and GCMT thrust earthquakes. Note the contiguous band of earthquakes along the southern Mariana trench and the cessation of this band where large residual bathymetric anomalies are observed. Inset shows the correlation between bathymetric anomalies and locations where serpentinite seamounts have been sampled (red pluses) [*Fryer*, 2012].

One unique characteristic of the Mariana arc is the presence of fore-arc seamounts associated with serpentinite mud diapirism [*Fryer et al.*, 1985; *Fryer and Smoot*, 1985; *Fryer and Fryer*, 1987; *Fryer et al.*, 1999; *Fryer*, 2012]. These seamounts typically occur 30–100 km west of the Mariana trench axis [*Fryer and Fryer*, 1987], have little or no magnetic signature [*Hussong*, 1982], and are associated with the upwelling of serpentinite muds formed in the mantle wedge as it is hydrated by fluids from the subducting plate [*Fryer*, 2012]. Locations where serpentinite seamounts have been sampled since 1981 are shown as red pluses in Figure 5c (inset) and we note that almost all are near large positive residual bathymetric anomalies. This correlation supports emplacement mechanisms whereby vertical tectonic movements and fracturing of the overthrusting plate required to accommodate subducting oceanic seamounts provides faults and planes of weakness along which diapirs of serpentinized ultramafics can rise [*Fryer et al.*, 1985; *Fryer and Smoot*, 1985].

5.3. Java

Offshore Java (Figure 6), the major bathymetric relief is associated with the Roo Rise oceanic plateau. The plateau has crustal thickness of 12–18 km [*Shulgin et al.*, 2011], a sharp eastern margin, and a tiered western margin. The inner boundary defines the western margin of the shallower central segment of the plateau, which can be tracked across trench axis and associated with a 2 km reduction in fore-arc water depth. The location of highs and lows within this elevated segment are contiguous with plateau physiography seaward of the trench axis. Northwest of the Roo Rise, a second residual bathymetric anomaly with amplitude $>$2 km in the outer fore arc is likely associated with an isolated subducting seamount.

The bathymetric anomalies we associate with subducting relief are limited by the 20 km depth contour of the subducting slab [*Hayes et al.*, 2012]. This contour is correlated with the location and geometry of the outer arc high, and the subducting slab–fore-arc-Moho intersection as constrained by wide-angle seismic-refraction profiles [*Kopp et al.*, 2002; *Planert et al.*, 2010; *Shulgin et al.*, 2011] (Figure 6a).

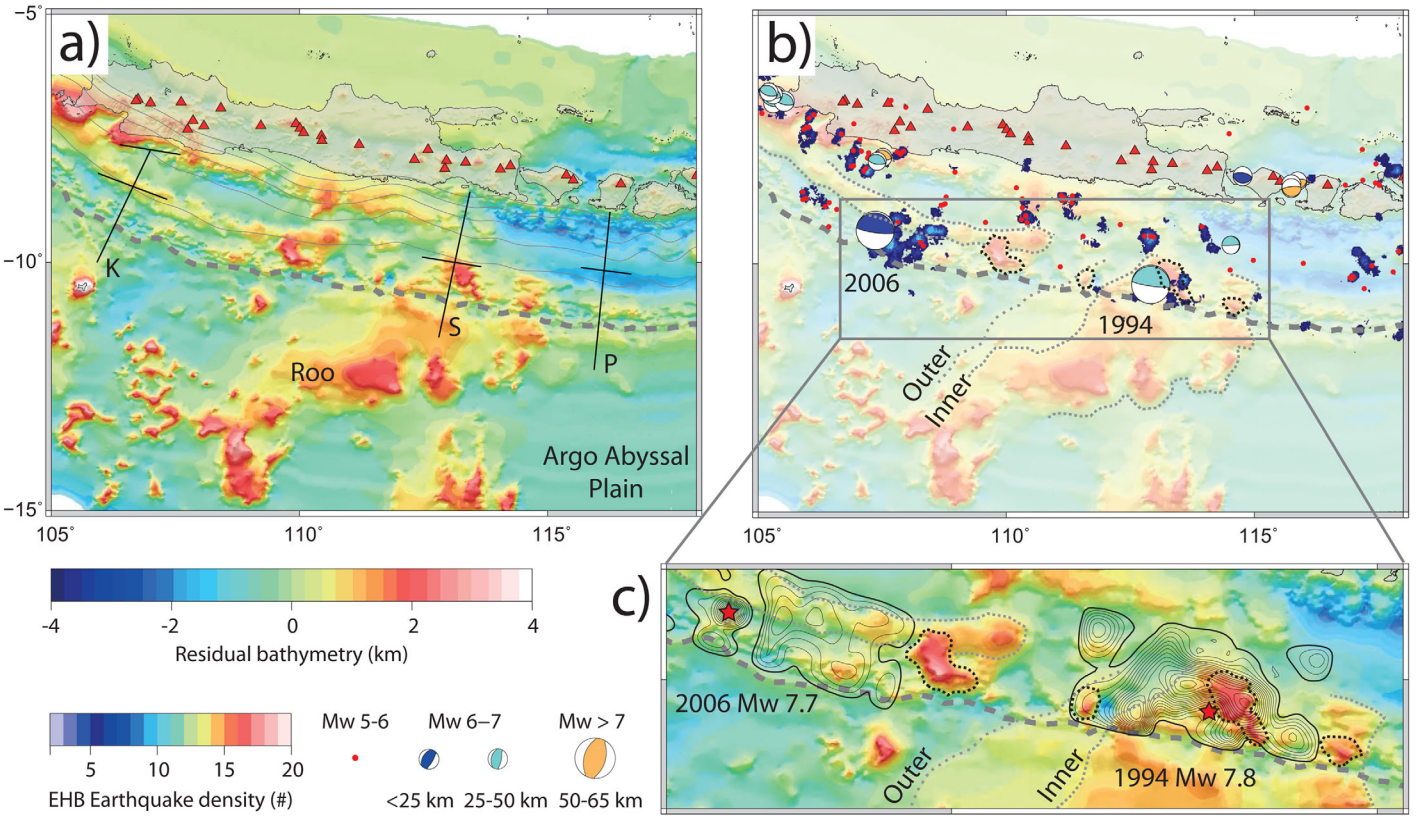

Figure 6. (a) Residual bathymetry for the Java subduction zone. Figure nomenclature as in Figure 4. Solid black profiles show the geometry of wide-angle seismic refraction profiles presented in K [*Kopp et al.*, 2002], S [*Shulgin et al.*, 2011], and P [*Planert et al.*, 2010]. Roo = Roo Rise oceanic plateau. (b) EHB/ISC earthquake density and GCMT thrust earthquakes. (c) Epicenters and coseismic slip distributions in the 1994 and 2006 tsunami earthquakes [*Bilek and Engdahl*, 2007].

Thrust earthquakes in Java are sparse, of highly variable mechanism and typically low magnitude. Only two earthquakes have Mw≥7, but these events are significant for being both tsunami earthquakes and widely cited examples of interactions between earthquakes and subducting seamounts [*Masson et al.*, 1990; *Abercrombie et al.*, 2001; *Bilek and Engdahl*, 2007]. Epicenters and distributed slip models for the 1994 (Mw 7.8) and 2006 (Mw 7.7) tsunami earthquakes from *Bilek and Engdahl* [2007] are shown in Figure 6c.

The 2006 earthquake propagated east with slip distributed between the trench and mantle-wedge corner. Residual bathymetry within the rupture area is typically low (<1 km), although a positive anomaly near the trench is correlated with a small increase in coseismic-slip (Figure 6c). The close proximity of the eastern rupture extent to a large residual bathymetric anomaly in the outer fore arc lead us to agree that the 2006 earthquake did not rupture or initiate near a subducting seamount, but was quite possibly arrested by one [*Bilek and Engdahl*, 2007].

The 1994 earthquake initiated on the southwestern flank of the largest residual bathymetric anomaly associated with the Roo Rise (Figure 6c). This earthquake propagated ~120 km east and west of the epicenter, extending between the trench axis and ~40 km depth. A detailed local correlation between coseismic slip and residual bathymetry is not observed, but we do interpret a regional correlation between the area of large coseismic slip and the western high-standing block of the plateau. Coseismic slip diminishes between the tiered western plateau boundaries and we interpret a second correlation between the western extent of coseismic slip and the outer boundary of the Roo Rise. We agree with existing links between the 1994 earthquake and subducting relief [*Abercrombie et al.*, 2001], but make this link with oceanic plateau rather than seamount subduction. This distinction may be significant given their contrasting modes of isostatic compensation and the lower height to length/width ratios of oceanic plateaus, which may influence megathrust roughness.

5.4. Japan

In 2011 offshore Honshu, Japan, the Mw 9.0 Tohoku-Oki earthquake ruptured ~400 km of strike [*Ide et al*., 2011; *Koketsu et al*., 2011; *Lay et al*., 2011; *Simons et al*., 2011]. The Pacific plate seafloor adjacent to this rupture area is smooth [*Wang and Bilek*, 2014], but further south and of significance to this study, subducting seamounts of the Joban seamount chain have been interpreted near the trench axis [*Lallemand et al*., 1989; *Nishizawa et al*., 2009] and >5 km beneath the fore arc [*Mochizuki et al*., 2008].

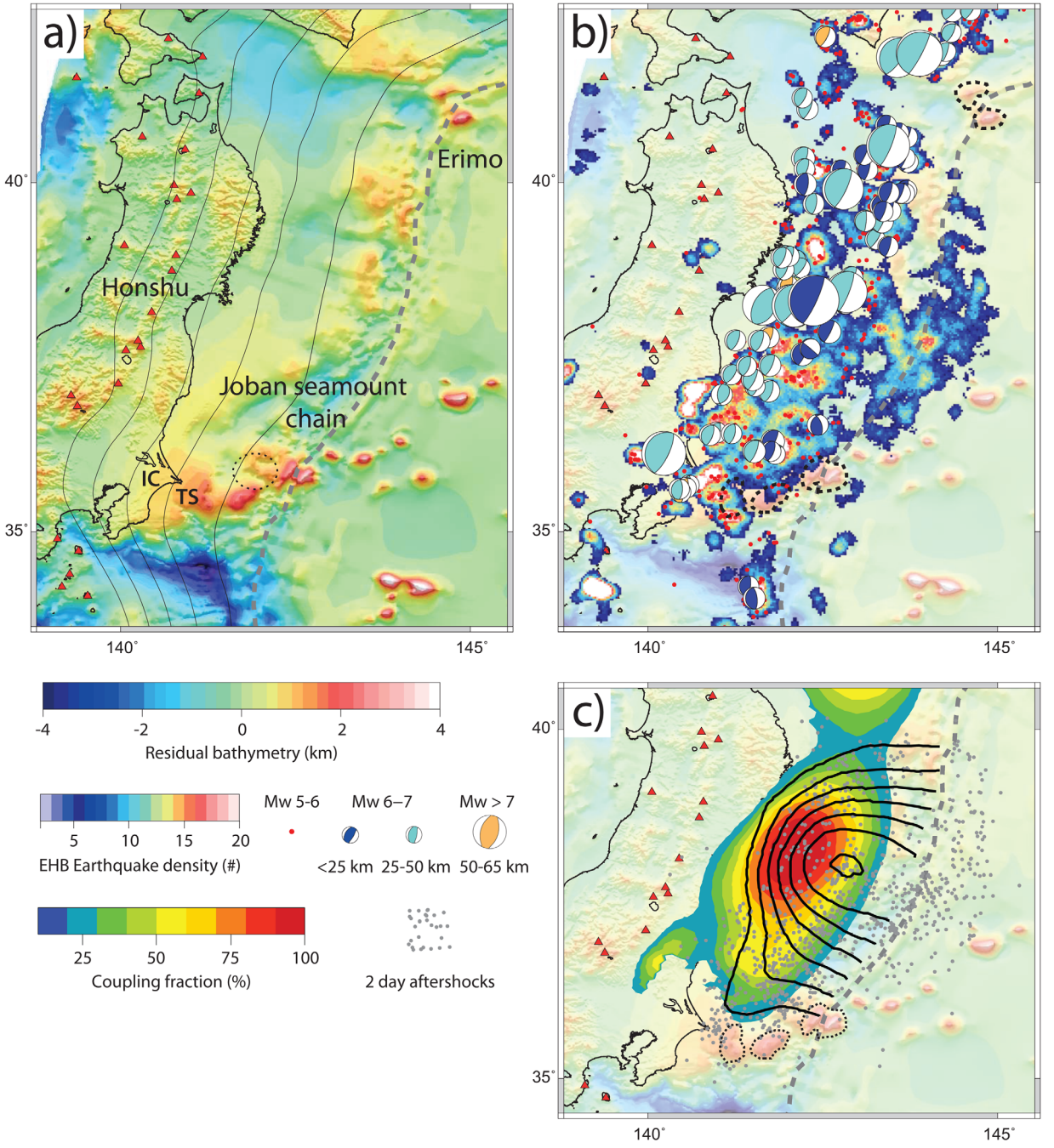

Figure 7. (a) Residual bathymetry for the Japan subduction zone. Figure nomenclature as in Figure 4. Dotted circle shows the interpreted position of a subducting seamount in *Mochizuki et al*. [2008]. IC = Inubo Cape. TS = Tyōshi spur. (b) EHB/ISC earthquake density and GCMT thrust earthquakes. (c) Geodetic coupling across the Japan-Pacific plate boundary and coseismic slip contours in the 2011 Tohoko-Oki earthquake (max slip 18 m) [*Loveless and Meade*, 2011]. Gray dots show 2 day aftershocks.

Residual bathymetry for the Japan trench is shown in Figure 7. In the north, Erimo seamount is observed seaward of the trench axis and a second residual bathymetric high (∼1.5 km) of similar dimensions has been associated with a subducting seamount [*Lallemand and Le Pichon*, 1987]. In the southern Japan trench, residual bathymetric highs with ∼2 km amplitude are aligned with unsubducted Joban seamounts and can be tracked >100 km landward of the trench axis. We tentatively interpret a third subducting seamount beneath the Tyōshi spur (TS), part of a regional positive anomaly extending from Inubo Cape (IC). The short-wavelength character of these anomalies is limited by the 30 km slab contour [*Hayes et al*., 2012] and near fore-arc crustal thickness estimates (∼25 km) [*Fujie et al*., 2013].

Most thrust earthquakes along the Japan megathrust are distributed between 10 and 50 km depth. In the EHB/ISC catalog, regions of low recent earthquake density are located: near the trench in northern Honshu where the outer fore arc is characterized by positive residual bathymetry; north of this region within a ∼70 km wide trench-normal bathymetric trough bounded by the Hokkaido continental slope break; and in regions of active seamount subduction. The seamount we interpret offshore Hokkaido is located in a region where the outer fore arc has regionally low-earthquake density. The subducting Joban seamounts have similarly low-earthquake density, but appear so adjacent to, and define the southward boundary of, a recently active segment of the megathrust.

In Figure 7c, we show the distribution of seismic coupling on the Pacific plate megathrust prior to the Tohoku-Oki earthquake, coseismic slip contours from inversion of horizontal displacements [*Loveless and Meade*, 2010], and the epicenters of aftershocks occurring within 2 days (gray dots). The region of Joban seamount subduction was characterized by low coupling before the earthquake, experienced no coseismic slip, and almost all aftershocks occurred on the megathrust to the north. These observations strongly support the suggestion of *Wang and Bilek* [2014] that Joban seamounts subduct via aseismic creep and may have acted as a barrier to the southward propagation of the Tohoku-Oki earthquake. The absence of large amplitude residual bathymetric anomalies in the center or northern region of the rupture zone make it unlikely subducting seamounts were associated with either the nucleation or northern termination of earthquake rupture [*Zhao et al*., 2011].

5.5. Kamchatka

Residual bathymetry for Kamchatka and the western Aleutians is shown in Figure 8. This grid is generated by calculating the average trench-normal profile from Kamchatka, but extending the removal of this profile further east and west along the western Aleutian and Kuril trenches, respectively. The subducting Emperor seamount chain can be identified as a 1–2 km high bathymetric anomaly ∼200 km landward of the trench axis and beneath the Kronotsky peninsula (KP in Figure 8a). The landward extent of this anomaly is coincident with the ∼40 km slab contour (Figure 8a), and is close to crustal thickness estimates (30–40 km) along the east coast of Kamchatka from gravity measurements, active source seismic [*Bogdanov and Khain*, 2000] and receiver function modeling [*Levin et al*., 2002].

In the 20th century, the Kamchatka megathrust has ruptured in six large (Mw ∼7), three great (Mw ≥8), and one giant (1952 Mw 9.0) earthquake (Figure 8c) [*Bürgmann et al*., 2005]. The region adjacent to the subducting Emperor seamount chain ruptured most recently in the 1997 Mw 7.8 Kronotsky earthquake, which propagated entirely southwest from an epicenter near the subducting ridge flank. Aftershock distributions for older events are uncertain, but these also suggest rupture extents restricted to one side of the subducting ridge, which appears a barrier to rupture propagation. Inversion of horizontal GPS velocities show the region of the subducting Emperor seamount chain to be strongly coupled [*Bürgmann et al*., 2005].

The black line in Figure 8b shows the small circle best fitting the locations of Kamchatka arc volcanoes [*England et al*., 2004]. Where the Emperor/Meiji seamounts subduct, arc volcanoes are located ∼50 km further landward and have residual bathymetry (∼4 km) at least 1 km higher than adjacent arc segments. Geochemical data [*Keller et al*., 2000; *Cottrell and Tarduno*, 2003], the change in physiography of the seamount chain, and the reduction in width of the flexural moat suggest the Hawaiian hotspot may have been close to a spreading ridge during the formation of Detroit seamount. Subduction of the Emperor seamount chain may thus be more analogous to aseismic ridge subduction, other examples of which are discussed below.

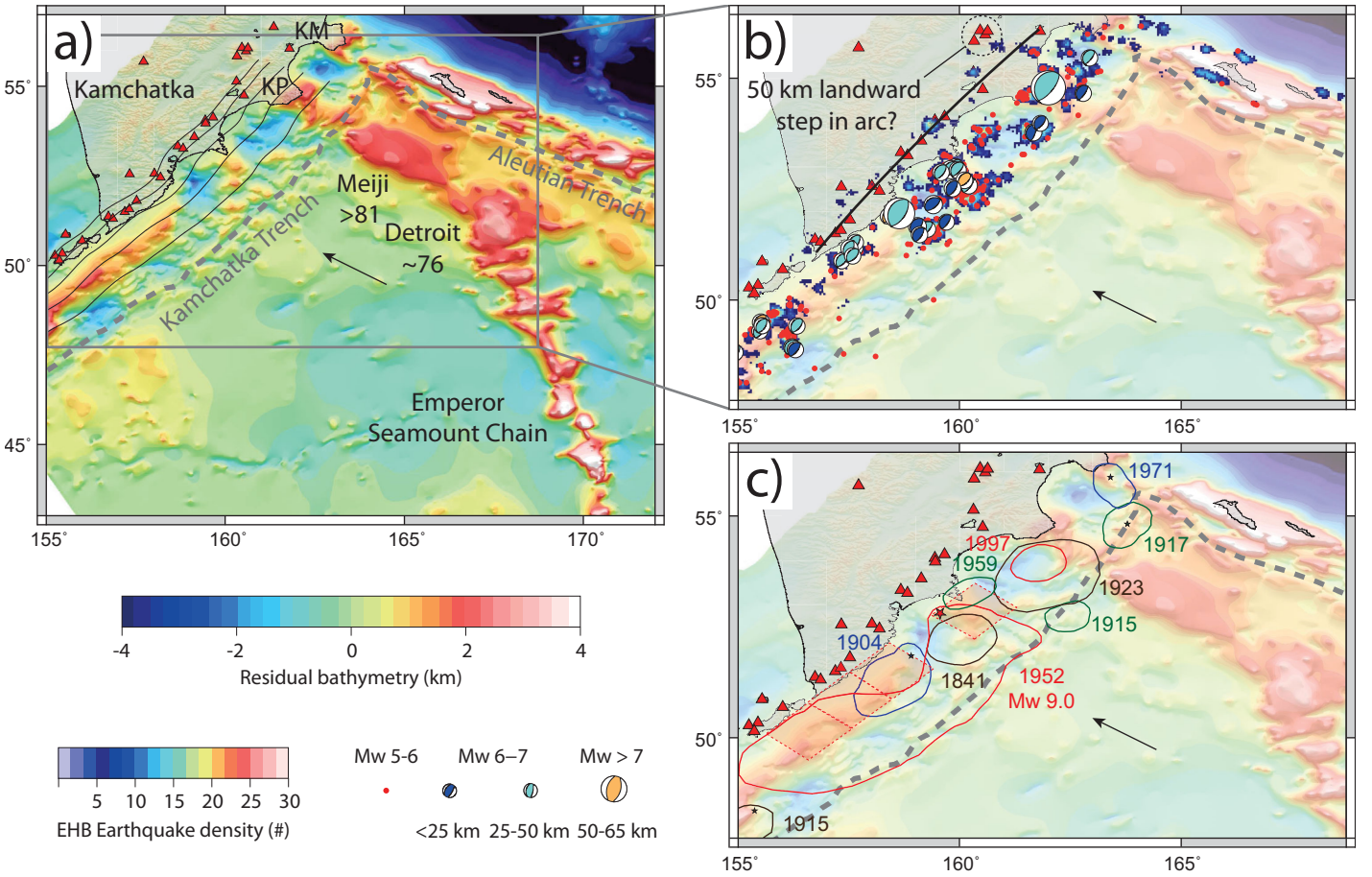

Figure 8. (a) Residual bathymetry for the Kamchatka subduction zone. Figure nomenclature as in Figure 4. The oldest extant seamounts are Detroit (75.8 ± 0.6 Ma) and Meiji (>81 Ma) [*Tarduno et al*., 2003; *Duncan and Keller*, 2004; *Clouard and Bonneville*, 2005]. KR = Kronotsky Peninsula. KM = Kamchatka Peninsula. (b) EHB/ISC earthquake density and GCMT thrust earthquakes. (c) Coseismic slip/aftershock zones of large earthquakes (modified from *Bürgmann et al*. [2005]. Red-filled squares show fault segments accommodating >6 m of slip in the 1952 Mw 9.0 earthquake from tsunami waveform inversion [*Johnson and Satake*, 1999].

6. Aseismic Ridges

6.1. South-America

The Nazca plate subducts beneath South America at rates increasing from ~54 mm yr^{-1} beneath Ecuador and Columbia to ~80 mm yr^{-1} beneath southern Chile [*DeMets et al*., 2010]. The active Chile Rise intersects the margin near 45°S and to the north, many of the fracture zones, seamounts, and aseismic ridges on the Nazca plate have been related to persistent seismogenic segment boundaries [*Bilek*, 2010; *Sparkes et al*., 2010] or the dynamics of individual earthquakes [*Barrientos and Ward*, 1990; *Robinson et al*., 2006]. The two largest bathymetric reliefs are the Nazca and Carnegie aseismic ridges (Figure 9).

Seaward of the trench, the Carnegie Ridge has residual bathymetry up to 3 km in height, crustal thickness of 14 km [*Graindorge et al*., 2004], and a width increasing toward the trench axis from 100 km to ~300 km. Over an identical width, the adjacent fore arc has residual bathymetry of similar amplitude (2–3 km). The surficial expression of the subducting ridge is strongest across the outer fore arc and diminishes entirely within 90 km of the trench axis. There is no residual bathymetric expression of the Carnegie Ridge across the inner fore arc, but further landward and analogous to observations made in Kamchatka (Figure 8b), we note that both the width (~100 km) and elevation (residual bathymetry >2km) of the volcanic arc increases by a factor >2 relative to adjacent regions.

The Grijalva fracture zone defines the southern boundary of the shallower northern segment of the Nazca plate, corresponding to a more seismically active segment of the megathrust. Where the Carnegie ridge

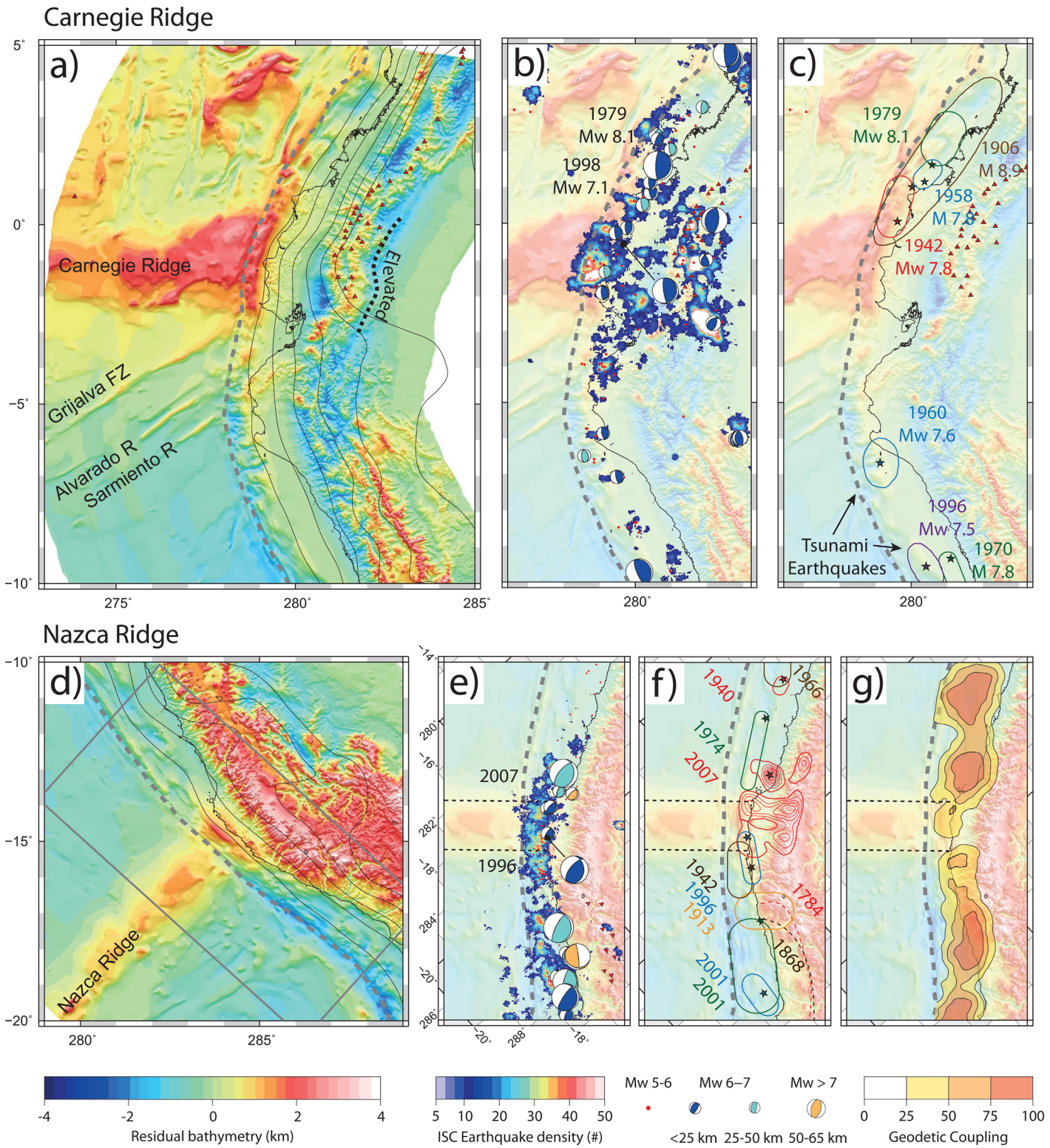

Figure 9. Aseismic ridge subduction beneath South America. Figure nomenclature as in Figure 4. (a) Residual bathymetry where the Carnegie Ridge subducts. (b) ISC earthquake density and GCMT thrust earthquakes. (c) Coseismic slip/aftershock zones of large earthquakes (modified from *Bilek* [2010]. (d) Residual bathymetry where the Nazca Ridge subducts. Gray box delimits the region shown in Figures 9e–g. (e) ISC earthquake density and GCMT thrust earthquakes. Dashed lines delimit the northern and southern Nazca ridge flanks. (f) Coseismic slip/aftershock zones of large earthquakes. 2007 earthquake slip distribution from [*Bilek*, 2010]. (g) Geodetic coupling from *Chlieh et al*. [2011].

subducts, thrust earthquakes with Mw $\geq$ 6 are located landward of residual bathymetric anomalies and have complex source-time functions [*Bilek*, 2010]. The southward propagation of large historical earthquakes in 1906 (Mw ~8.8) and 1942 (Mw 7.8) was limited by the northern ridge flank [*Kelleher*, 1972; *Collot et al*., 2004].

EHB earthquake density is regionally low along the Peru, Ecuador, and Columbia segments of the convergent plate boundary. The ISC catalog, in contrast, shows higher densities where the Carnegie ridge is subducted, particularly in the outer fore arc near subducting ridge flanks, and near the volcanic arc (Figure 9b). The different magnitude ranges over which the EHB (mb $\geq$ 3) and ISC (mb $\geq$ 2) bulletins are constructed may suggest this increase in density is from small earthquakes.

The Nazca aseismic ridge is ~200 km wide, trench-normal, and has a residual bathymetry high of up to 1.5 km amplitude. Across the fore arc, the surficial expression of the subducting ridge has amplitude up to 2 km, is strongly limited to the outer fore arc and has a width well correlated with ridge physiography seaward of the trench. The volcanic arc terminates east of this region and although the Peruvian Andes have residual bathymetry up to 1 km higher than the adjacent region further north, it is not clear if this additional elevation is associated with ridge subduction.

Thrust earthquakes are frequent where the Nazca ridge subducts, most recently occurring in 2007 (Mw 8.0) near the north-western ridge flank. From inversion of body waves, *Bilek* [2010] model 2 m of slip near the epicenter and identify a second broad zone with ~1 m of slip aligned with the north-western ridge flank (Figure 9f). Low slip is modeled southeast of this zone, is not required to fit InSAR and GPS observations [*Chlieh et al*., 2011] and at depths <50 km the north-western Nazca ridge flank acted as a barrier to rupture propagation.

The southern flank of the Nazca ridge ruptured in 1942 (Mw 8.2) and 1996 (Mw 7.7). The 1942 event is suggested to be complex, with southward rupture propagation and significant moment release away from the Nazca ridge [*Swenson and Beck*, 1996]. The 1996 earthquake had an epicenter on the southern ridge flank and also propagated south rebreaking the deeper portion of the 1942 rupture area [*Chlieh et al*., 2011]. Neither earthquake propagated north of the ridge crest and the south-eastern ridge flank may also act to limit rupture propagation.

Subduction of the Nazca ridge is similarly correlated with an increase in ISC earthquake density (Figure 9e). The highest densities are near the flanks of the subducting ridge and are separated by a region of lower density near the ridge-crest.

Bilek [2010] associate the 2007 earthquake with a gap left since the 1687 earthquake, but note that the $\leq$2 m of coseismic slip is an order of magnitude less than the 20 m of relative plate motion accrued. From interseismic GPS observations, *Chlieh et al*. [2011] show the megathrust immediately overlying the subducting Nazca ridge is weakly coupled (creeping) and up to 60% of relative plate motion may be accommodated aseismically (Figure 9g).

Intermediate magnitude thrust events in both of these collision zones are more complex, have longer durations [*Bilek*, 2010] and are consistent with observations of rupture complexity in large events [*Swenson and Beck*, 1996; *Bilek*, 2010]. These observations are interpreted as reflecting the structural complexity and lower rigidity of the megathrust, and correlation with elevated earthquake densities and geodetic observations of low coupling may suggest that upper plate deformation and small earthquakes accommodate a significant proportion of relative plate motion where aseismic ridges are subducted.

6.2. Central-America

The subducting plate offshore Costa Rica is extremely rough hosting the Cocos Ridge, Panama fracture zone, and >10 ridge flanking seamounts. Residual bathymetry in this region is shown in Figure 10.

Seaward of the trench axis, the Cocos Ridge is ~200 km wide, ~2 km high, and has thicknesses up to 20 km [*Walther*, 2003]. Residual bathymetric anomalies associated with this ridge, and a margin normal ridge and trough associated with the Panama fracture zone, are strongly limited to the outer fore arc within 40–60 km of the trench axis.

Landward of the Cocos Ridge, the Cordillera de Talamanca (CDT) has residual bathymetry >2 km, is a factor >2 wider than the adjacent Cordillera de Guanacste (CDG) and Serrania de Tabasara (SDT), and is the highest mountain range in Central America (Figure 10a). This observation is analogous to the wider and higher volcanic arcs landward of the Emperor/Meiji and Carnegie ridges.

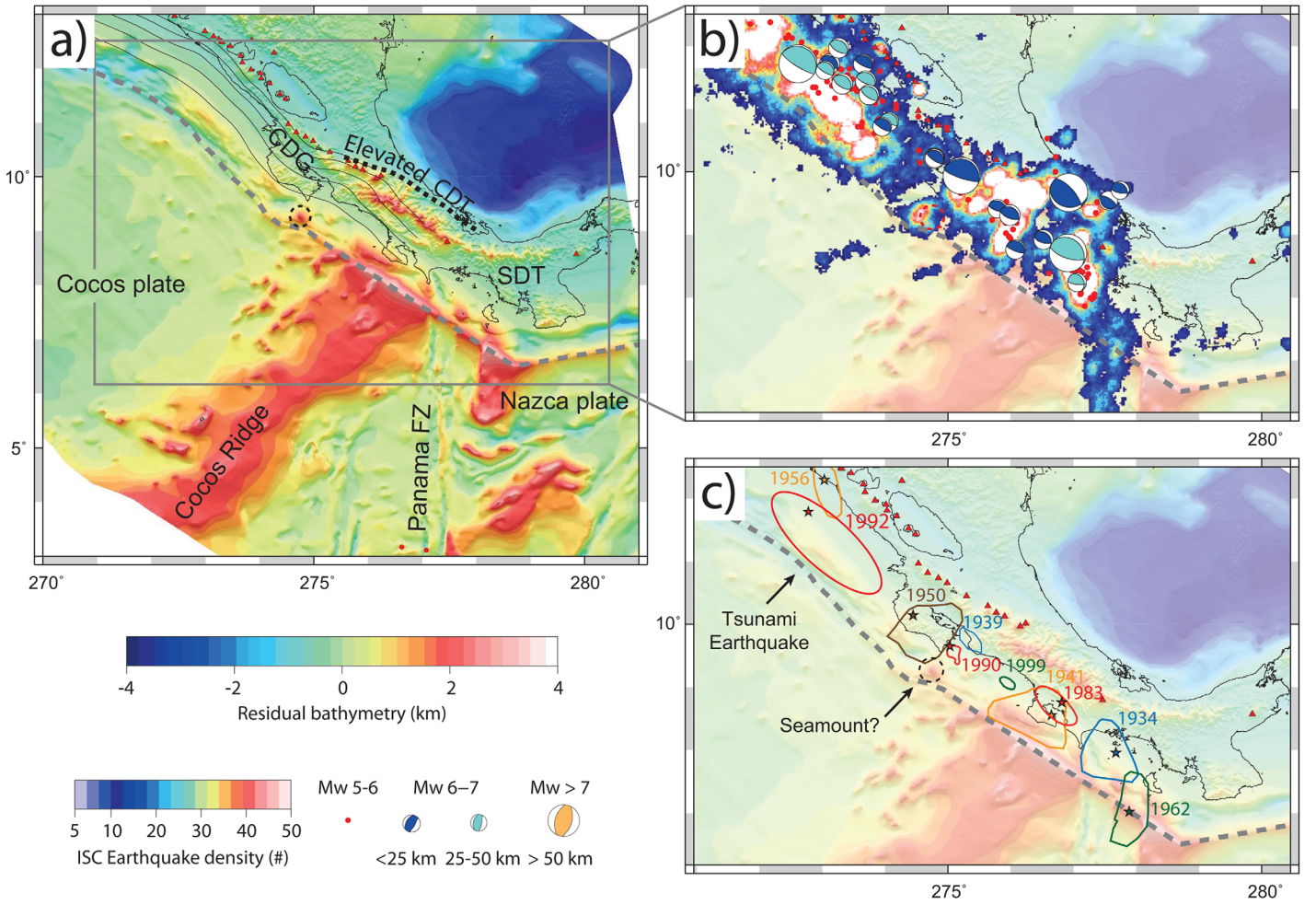

Figure 10. Aseismic ridge subduction beneath Central America. (a) Residual bathymetry where the Cocos Ridge subducts. Figure nomenclature as in Figure 4. (b) ISC earthquake density and GCMT thrust earthquakes. (c) Coseismic slip/aftershock zones of large earthquakes [*Kelleher et al.*, 1973; *Kanamori and Kikuchi*, 1993; *Protti et al.*, 1995; *Tajima and Kikuchi*, 1995; *Bilek et al.*, 2003].

Most thrust earthquakes are distributed across the inner fore arc and landward of large residual bathymetric anomalies (Figure 10b). Exceptions are a cluster of events aligned with the Panama fracture zone; and a second smaller cluster located west of a conical ~2 km residual bathymetric high (circled in Figure 10) that is likely associated with a subducting seamount. A Mw 7.0 event occurred <50 km downdip of this high in 1990 [*Bilek et al.*, 2003] and it is possible this seamount, or a deeper subducting geometrical irregularity, contributed to the termination of rupture in the 1950 Mw ~7.7 earthquake near the eastern Nicoya Peninsula (Figure 10c)[*Protti et al.*, 1995].

Historical earthquakes landward of the Cocos Ridge occurred in 1941 (M ~7.7) and east of the Panama fracture zone in 1934 (M ~7.7) [*Kelleher et al.*, 1973]. Source time functions for recent events in 1983 (Mw 7.4), 1990 (Mw 7.0), and 1999 (Mw 6.9) are complex, consisting of multiple subevents, often at different depths and/or with different focal mechanisms [*Bilek et al.*, 2003]. This complexity is in stark contrast to the simple source time function associated with the 1992 (Mw 7.7) tsunami earthquake offshore Nicaragua [*Kanamori and Kikuchi*, 1993], which *Wang and Bilek* [2011] interpret as reflecting the roughness of the subducting plate and the structural complexity of the megathrust. The distribution of residual bathymetric anomalies supports this interpretation.

ISC earthquake density is displayed in Figure 10b. Although similar in magnitude to the adjacent Nicaragua segment, large earthquake densities offshore Costa-Rica extend further downdip and are organized in two approximately margin normal bands. Analogous to the Carnegie and Nazca ridges, the northwestern band

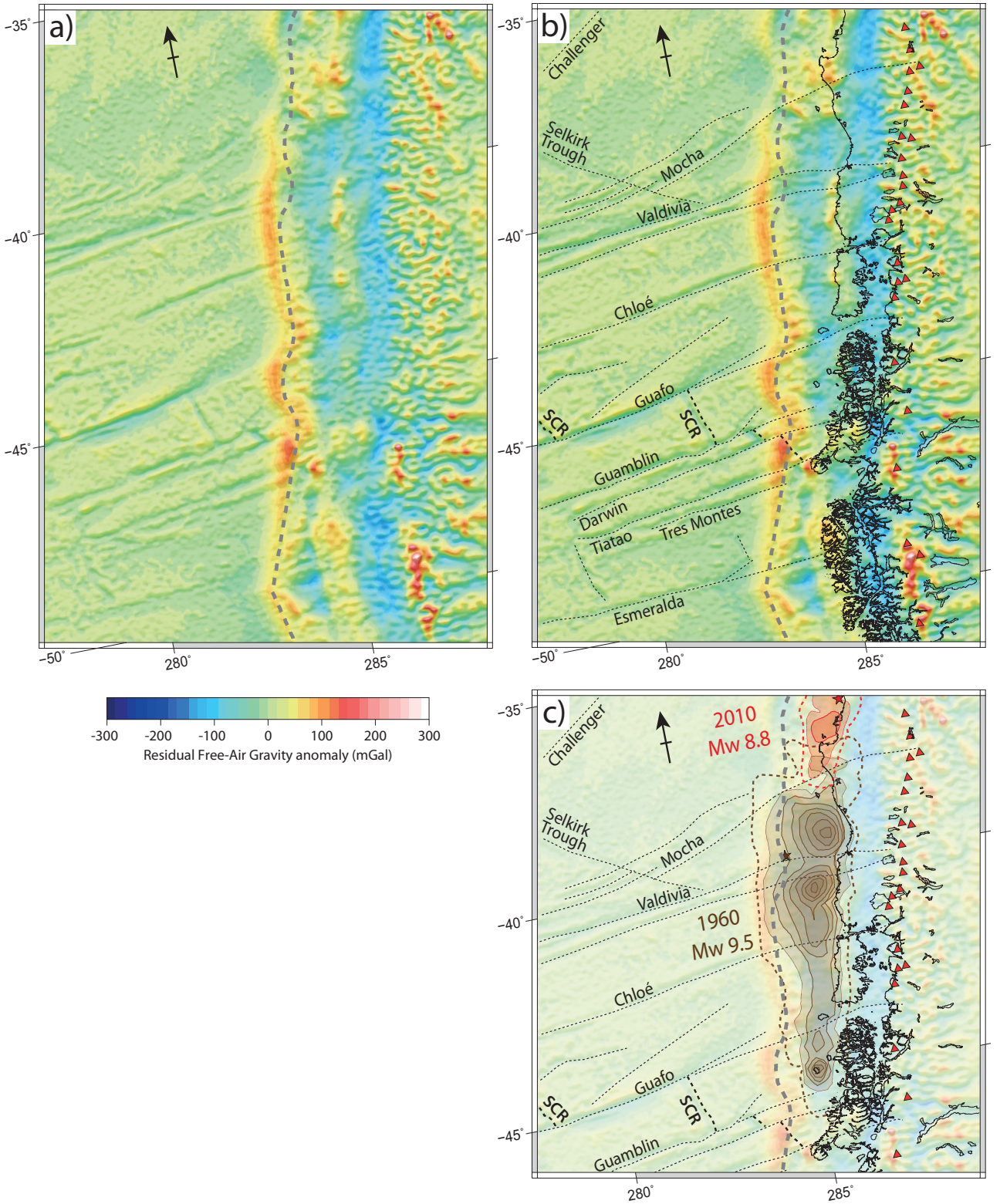

Figure 11. (a) Residual free-air gravity anomaly for southern the Chile subduction zone. (b) Interpreted with historically active volcanoes [*Simkin and Siebert*, 2002], the coastline (light gray) and interpretations of subducting fracture zones. Note the correlation with steps in the geometry of the trench and the morphological segmentation of the fore arc. SCR = South Chile Rise. (c) Slip distribution in the 1960 Chile [*Barrientos and Ward*, 1990] and 2010 Maule [*Delouis et al*., 2010] earthquakes.

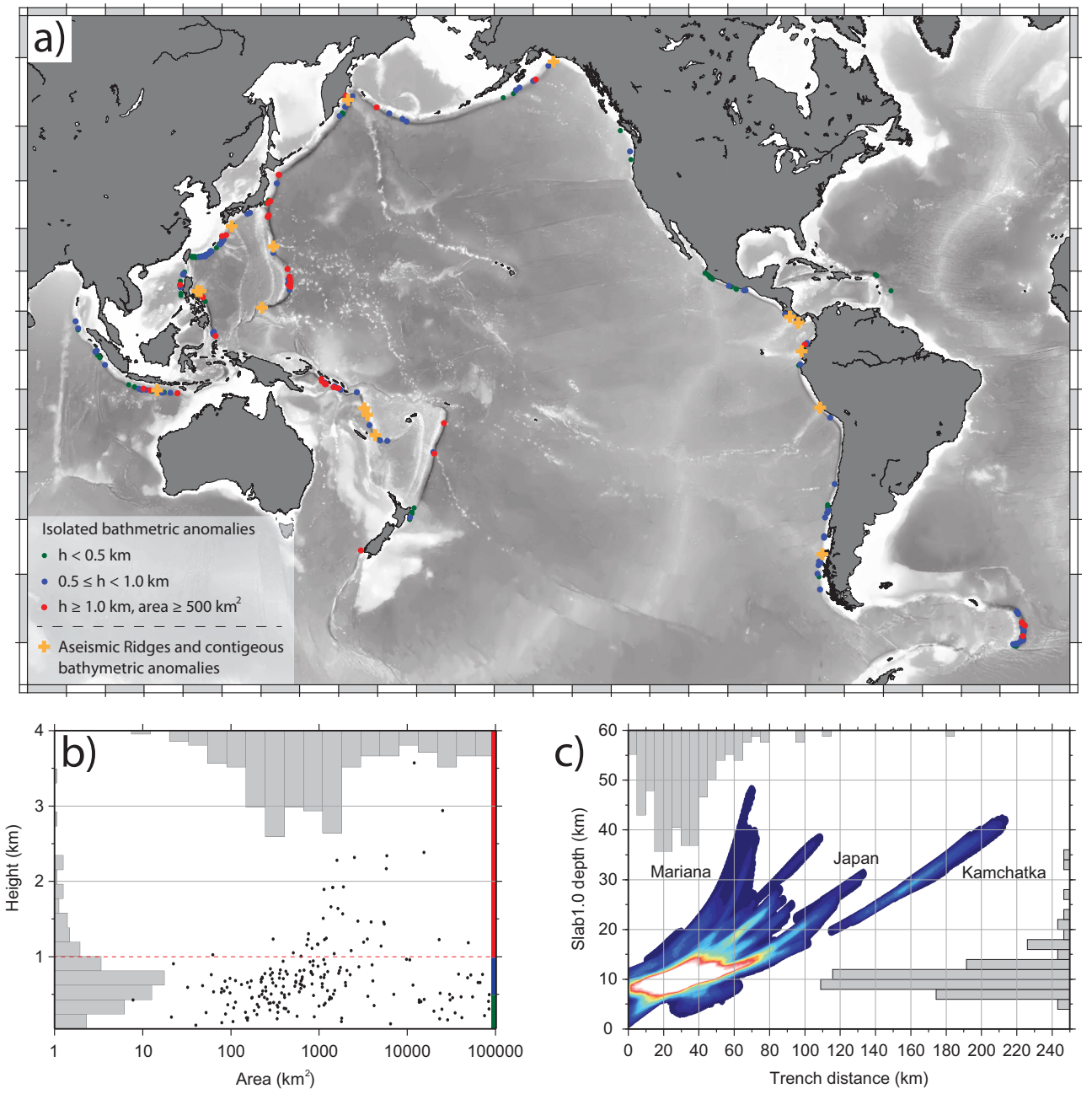

Figure 12. Global subducting relief. (a) Distribution of residual bathymetric anomalies possibly associated with subducting relief. See Legend. (b) Histograms and scatter plots showing the height (h) and area of isolated residual bathymetric anomalies potentially associated with subducting seamounts. (c) Histograms and point density plot showing the distribution of isolated residual bathymetric anomalies with respect to trench distance and SLAB1.0 depth [*Hayes et al.*, 2012].

is spatially and geometrically correlated with the flank of the Cocos ridge, and a region of lower earthquake density is near the subducting ridge crest. The North-South strike of the southeastern band is aligned with the subducting Panama fracture zone, which may define the southeastern margin of the Cocos ridge at depth. No large earthquakes are known to have ruptured across the flanks of the subducting Cocos ridge.

7. Fracture Zones: Southern Chile

Fracture zones are aseismic, off-axis, traces of the transform faults that segment mid-ocean ridge systems. The sediment cover of ocean basins is often sufficient to bathymetrically obscure fracture zones; however,

basement topography and variations in crustal thickness and petrology usually result in a clear expression in the gravity field [*Robb and Kane*, 1975; *Fox et al*., 1976; *Prince and Forsyth*, 1988; *Matthews et al*., 2011].

In Southern Chile, the active Chile Rise is subducted near 45°S and a dense network of ENE striking fracture zones in the adjacent Nazca and Antarctic plates are clearly expressed in grids of residual free-air gravity anomalies (Figure 11). The largest fracture zones (e.g., Mocha, Valdivia, Guafo, Darwin) are correlated with up to 50 km steps in the location of the trench axis and can be interpreted up to 300 km further landward (Figure 11b).

The obliquity of most fracture zones with respect to margin-strike decreases across the trench axis in response to the dip of the subducting slab. Across the fore arc, they are correlated with boundaries between structural segments characterized by positive or negative/near-zero free-air gravity anomalies and cusps or transitions in the physiography of the coastline.

Figure 11c shows the distribution of slip in the 1960 Mw 9.5 Chilean earthquake [*Barrientos and Ward*, 1990]. This giant event ruptured the megathrust between the Mocha and Guamblin fracture zones and the northern and southern rupture limits are coincident with shallower fore-arc segments, the latter reflecting subduction of the Chile Rise (SCR). The distributed slip model shows three main asperities and *Barrientos and Ward* [1990] noticed that the boundaries between these asperities, and the northern and southern rupture limits, were close to the projected locations of fracture zones. Our constraints on fracture zone geometries and observations of margin segmentation support the suggestion of *Barrientos and Ward* [1990] that fracture zones may be an important source of margin segmentation along the southern Chile fore arc.

The influence of fracture zones on the segmentation of subduction boundaries is further demonstrated by observations in the Aleutian and southern Kuril Islands presented in part 2 of this study.

8. Discussion

It has long been suggested that the tectonic structure of the subducting plate exerts a strong influence on interseismic and coseismic deformation in subduction zones [*Kelleher and McCann*, 1976; *Spence*, 1977], but the physical and mechanical processes by which tectonic features subduct and the seismological consequences of this interaction remain a subject of debate and contrasting mechanical models have been proposed. One model suggests seamounts are accreted, either by decapitation at some level or by shearing along their base [*Cloos*, 1992; *Cloos and Shreve*, 1996], and act as seismic asperities generating large earthquakes within the seismogenic zone [*Cloos*, 1992; *Scholz and Small*, 1997]. An alternate model, proposed by *Wang and Bilek* [2011, 2014], posits that seamounts subduct more or less intact, with the development of a dense fracture network near and above the subduction interface resulting in fault conditions favorable for many small earthquakes and creep, and unfavorable for the nucleation of large earthquakes. It is not possible in our grids to discriminate between actively subducting and accreted relief, but the morphology and spatial distribution of bathymetric anomalies we interpret within fore arcs, and the relationships they show with recent seismicity, may provide constraints discriminating between these models.

8.1. Distribution and Character of Subducting Seamounts

From residual bathymetric grids for all subduction zones on Earth, >200 bathymetric anomalies are identified within fore arcs that may be associated with subducting relief. Isolated and irregular bathymetric anomalies are interpreted as subducting seamounts, most of which are similar in wavelength, amplitude, and morphology to seamounts located seaward of the trench axis.

The area and height (h) of each bathymetric anomaly is estimated by determining the deepest closed residual bathymetric contour circumscribing the anomaly, before calculating the area and depth difference between the basal contour and anomaly peak. Most anomalies have height <1 km (Figure 12b) and their spatial distribution is colored for height and shown in Figure 12a. Anomalies with h≥1 km and area ≥500 km^2 are shown as red dots (N=36) and, coupled with aseismic ridges (yellow pluses N>10), represent our most confident interpretations of subducting relief. Anomalies with 0.5≥h>1 km (N=96) and h<0.5 (N=72) are shown as blue and green dots, respectively and, although more speculative than larger anomalies, in many regions (e.g., Ryukyu, Mexico) the lower amplitude is consistent with seamount heights seaward of the trench axis. A strong correlation is observed between locations of residual bathymetric anomalies and the bathymetric character of the adjacent subducting plate seafloor, which supports

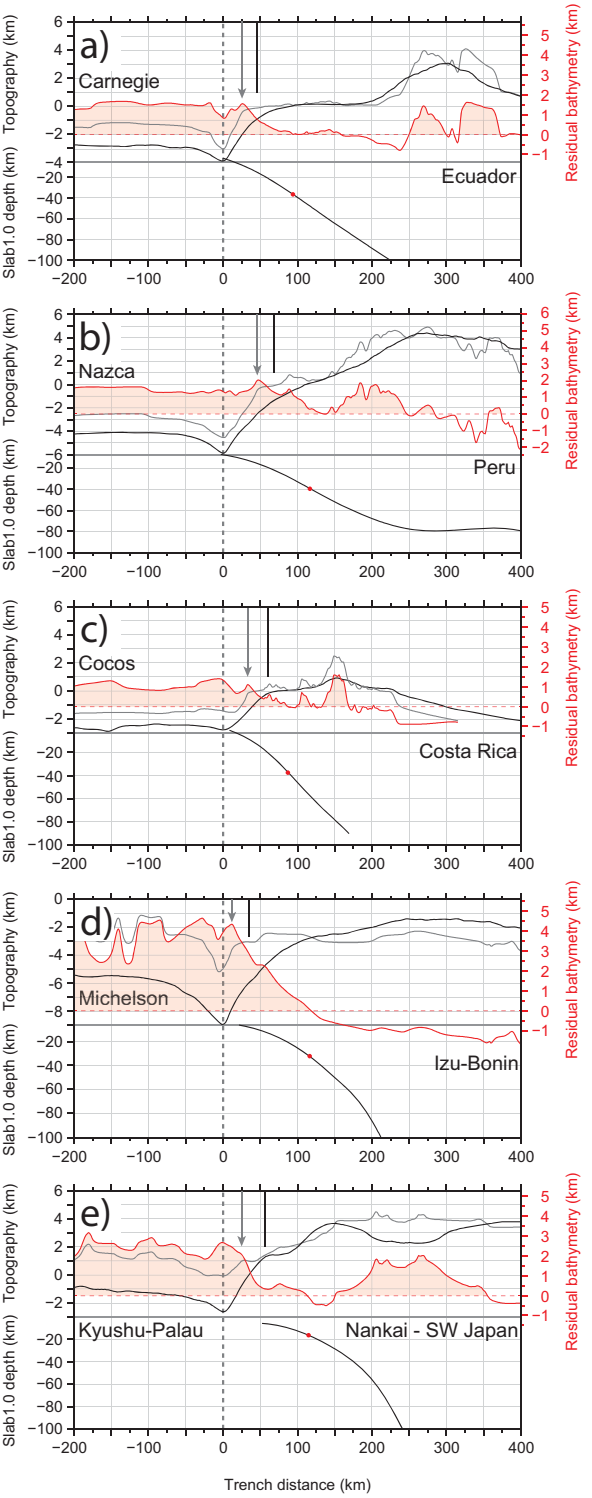

Figure 13. Aseismic ridge profiles. Profiles showing topography (gray), ensemble average topography (black), and residual bathymetry (red = gray-black) across five regions of aseismic ridge subduction. The subducting SLAB1.0 geometry is shown in black (vertical scale compressed) [*Hayes et al.*, 2012]. Vertical black and gray (with arrow) lines mark the interpreted position of the trench-slope break for the ensemble average and residual bathymetric profiles, respectively, and illustrate the reduction in width of the outer-fore arc.

assumptions made in existing regional studies of the influence of bathymetric relief on seismogenic behavior. A catalogue containing the location, height, area, and volume of each bathymetric anomaly is provided in supporting information.

The histograms in Figure 12c show the distribution of residual bathymetric anomaly peaks with respect to slab-depth and trench distance. Most anomaly peaks (95%) are located within 70 km of the trench axis and above regions where the subducting SLAB1.0 depth is less than 17 km [*Hayes et al.*, 2012]. The underlying density plot reflects the full area occupied by all residual bathymetric anomalies (excluding aseismic ridges) and reveals a similar restriction of most anomalies to the shallow and near trench region of subduction zones. In Japan and Kamchatka, bathymetric anomalies in line with the Joban and Emperor seamount chains are identified $>$100 km landward of the trench axis, associated with SLAB1.0 depths $\geq$30 km. These large lateral extents may reflect the shallow trajectory of the subducting Pacific Plate and/or fore-arc crustal thickness.

Density plots showing the distribution of slab-depths and trench distances associated with residual bathymetric anomalies for each active margin segment are shown in supporting information. Where known, the depth of the fore-arc Moho is shown as a dashed red line, which in Tonga, Java, and Mariana appears to bound the landward limit of most residual bathymetric anomalies. These observations are consistent with the lack of surface uplift observed above a possible deep (30–40 km) subducting seamount imaged below the fore-arc Moho in Sumatra [*Singh et al.*, 2011]. The isolated and irregular nature of subducting seamounts makes it difficult to reliably constrain the dip-parallel extent of subducting relief. This difficulty is significantly reduced for the case of aseismic ridge subduction.

8.2. Character of Aseismic Ridge Subduction

Subducting aseismic ridges appear subject to similar observation limits as seamounts and large residual bathymetric anomalies are strongly limited to the outer fore arc. In contrast to seamounts, however, where aseismic ridges subduct it is simpler to assume the location, width, and height of the subducting

bathymetric relief from ridge physiography seaward of the trench axis; and in most cases, the assumption that subducting ridges extend beyond the outer fore arc is likely to be similarly valid. The residual bathymetric expression of aseismic ridges can thus be interpreted as constraining the spatial limits over which subducting bathymetric anomalies directly influence fore-arc morphology, enabling the physical controls on these limits to be considered.

Figure 13 shows profiles of bathymetry (grey solid line) and residual bathymetry (filled red line) traversing five subducting aseismic ridges. The ensemble-average profile, calculated across the ∼250 km of trench either side of the ridge, is shown in black and reflects the mean structure of the trench slope in the absence of subducting relief. The subducting SLAB1.0 geometry is also shown in black (note different depth scale) [*Hayes et al*., 2012]. These profiles reveal the contrasting architecture of the fore arc in regions of aseismic ridge subduction.

In general, the amplitude of residual bathymetric anomalies is maintained in the trench axis. The geometry of the seaward trench slope is parallel to the ensemble-average profile and the outer fore arc is similarly elevated. The trench-slope break, however, is located 45–70 km (factor >2) nearer the trench. Relative to the ensemble-average profile, the outer fore arc is steeper and the inner fore arc is shallower/near-horizontal resulting in a gradual dip-parallel reduction in the bathymetric expression of the ridge. We thus observe a strong correlation between the location of the trench-slope break, which occurs 10–50 km landward of the trench axis and above SLAB1.0 depths of 5–15 km, and the landward limit of large residual bathymetric anomalies. The amplitude reduction in ridge expression across the inner fore arc occurs over ∼50–100 km and residual bathymetric anomalies converge with ensemble average profiles, indicating there is no expression of the subducting ridge, 80–120 km from the trench axis.

In Costa-Rica, Ecuador, and Kamchatka, the active volcanic-arc landward of subducting ridges is elevated relative to adjacent regions by 1.5–2.0 km. The top of the slab beneath the arc/highlands is typically $>$60 km deep and near-arc uplift is juxtaposed against the notable absence of residual bathymetric anomalies associated with subducting relief across the inner fore arc.

8.3. Implications for Mechanical Models of Bathymetric Relief Subduction

8.3.1. Interpretation of Aseismic Ridge Profiles

The along-strike extent of outer fore-arc and near-arc uplift indicates both are clearly related to aseismic ridge subduction, but what might the margin normal transitions illustrated in Figure 13 reflect physically with regard to the mechanics of bathymetric relief subduction and the properties of the overthrusting wedge and/or megathrust? One simple interpretation comes from considering the influence of margin normal variations in rigidity on where and how the upper plate deforms, both to accommodate subducting relief and in response to stresses transmitted across the plate boundary.

Assuming steady slip of the plate interface against constant resistance, the classical critical wedge theory predicts a greater surface slope for a stronger basal fault and/or weaker wedge material [*Davis et al*., 1983; *Dahlen et al*., 1984]. The subduction interface beneath the outer wedge is unlikely to be stronger than beneath the inner wedge and we thus follow *Byrne et al*. [1988] in interpreting the structural contrast across the slope break as reflecting the relative strength of materials comprising the inner and outer fore arc. This interpretation is supported by inferences of rigidity contrasts from normalized thrust earthquake source durations [*Bilek*, 2010] and seismic velocities in north Chile [*Sallarès and Ranero*, 2005], the latter of which suggest declining pore-fluid pressure and less fracturing of the overthrusting plate across the inner fore arc. The gradient of the reduction in residual bathymetric amplitudes landward of the slope break (Figure 13) may reflect the length scale over which the rigidity of the upper plate increases, thereby increasing resistance to buoyancy-driven upward flexure above subducting relief, or may alternatively reflect the increasing dip of the subduction interface.

In Ecuador (Figure 9b), Peru (Figure 9e), and Costa-Rica (Figure 10b), thrust earthquakes with Mw$\geq$6 are located entirely landward of the trench-slope break and the large residual bathymetric anomalies of the outer fore arc. This distribution is consistent with dynamic Coulomb wedge theory, which associates the trench-slope break with the updip transition from aseismic velocity strengthening to seismogenic velocity weakening behavior on the subduction interface [*Wang and Hu*, 2006].

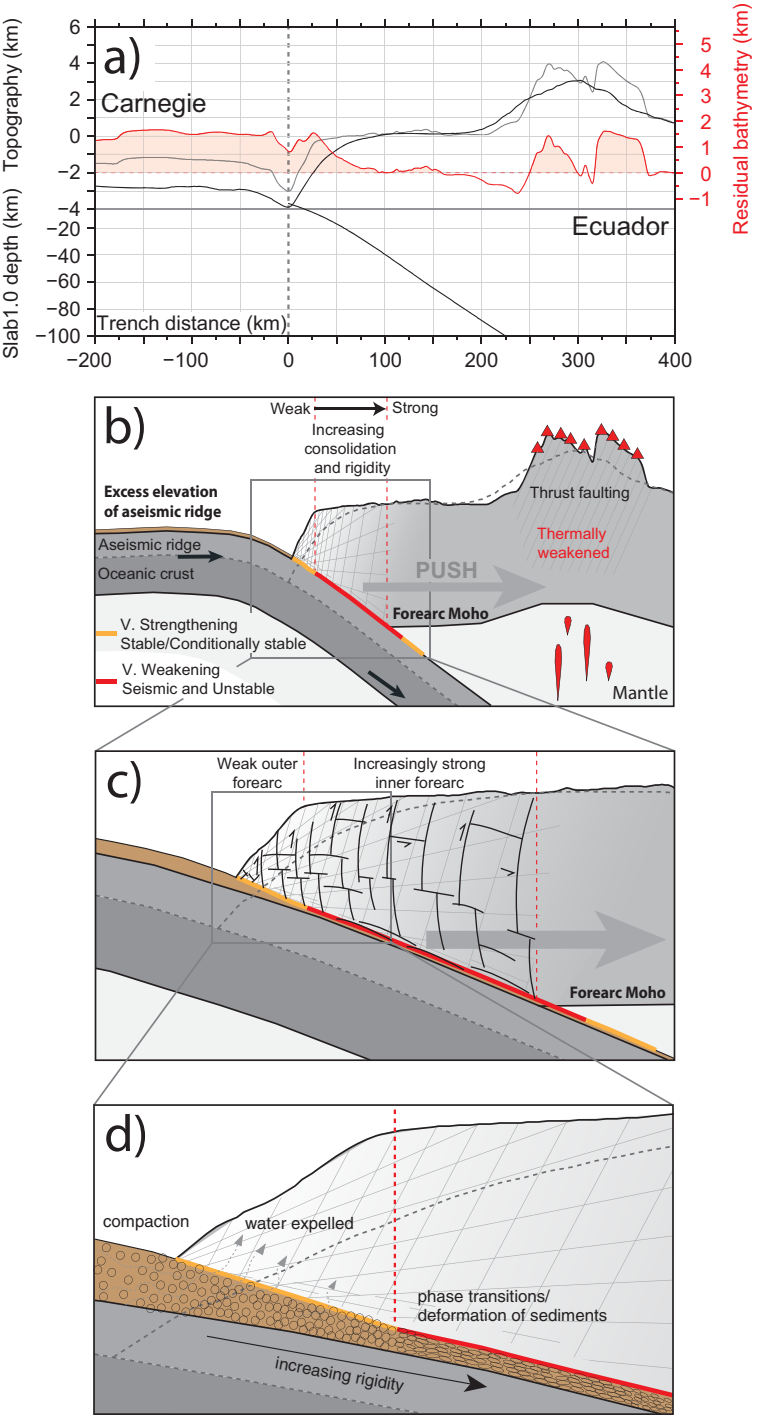

Figure 14. Cartoon illustrating one possible interpretation of the residual bathymetric expression of aseismic ridges. (a) Profiles showing topography (gray), ensemble average topography (black), and residual bathymetry (red = gray-black) where the Carnegie ridge subducts beneath Ecuador. (b) Near trench uplift is related to the weak and underconsolidated nature of near-trench material and its low resistance to uplift. Near arc uplift is related to the structural complexity of the megathrust and the higher stresses transmitted through the fore arc. These stresses are focused and drive deformation at the arc due to the higher heat flux and associated thermal weakening. (c) The slope break may define the outer boundary of the margin framework and/or, be coincident with the transition from velocity strengthening to velocity weakening behavior on the subduction interface. (d) At shallow depth, the megathrust slip regime and the physical properties of the overthrusting wedge may be significantly influenced by compaction and mineralogical phase changes in subducting sediments.

The subducting slab beneath volcanic arcs is typically 80–120 km deep [*England et al*., 2004; *Syracuse and Abers*, 2006] and in regions of aseismic ridge subduction always exceeds the thickness of overthrusting plates. In contrast to uplift of the outer fore arc, the presence of a mantle wedge makes it unlikely that the additional elevation of arcs is directly associated with the excess topography of subducting ridges and direct influences of this nature would be expected to also extend across the inner fore arc, which is not observed. An alternate explanation might be that the added thickness of subducting crust increases the volatile flux to the mantle wedge enabling a greater degree of partial melting, resulting in more arc volcanism and a larger arc. Landward of the subducting Emperor seamount chain, Klyuchevskoy is the most active arc volcano on Earth (Figure 8c), but this also is not our preferred interpretation. The forces that drive deformation at subduction zones are transmitted across the plate interface and we suggest near arc uplift may be related to the influence of bathymetric relief subduction on the magnitude of these forces.

In the "breaking through" model of *Wang and Bilek* [2011, 2014], the geometrical incompatibility of subducting relief is overcome by permanently deforming the surrounding rocks of both the subducting and overthrusting plates. At low temperature, the deformation is in the form of pervasive fracturing (Figure 14c), which is predicted by analog modeling [*Dominguez et al*., 1998; *Dominguez et al*., 2000], and likely reflected in the structural complexity of exhumed subduction zones [*Vannucchi et al*., 2006] and seismic images in regions of recent/ongoing seamount subduction [*Kodaira et al*., 2000; *Ranero and von Huene*, 2000; *von Huene et al*., 2000; *Bangs et al*., 2006; *Bell et al*., 2010]. Any change in fault geometry in the slip-direction acts to resist fault slip and one significant aspect of the breaking through model relates to the strength of the megathrust. Although creeping faults are typically considered to be weak, and locked faults considered strong, along a rough fault the breaking and wearing of geometrical irregularities within a broad and internally complex fracture network likely results in an integrated geometrical resistance against creep that is likely to be stronger than the locking stress of a smooth fault [*Wang and Bilek*, 2011, 2014]. Fault strength is linked to surface heat-flow by frictional heating and from heat-flow observations across 10 subduction zones, *Gao and Wang* [2014] show that rough creeping megathrusts dissipate more heat and therefore tend to be stronger than the smooth megathrusts that generate large earthquakes.

The stresses transmitted through the fore arc may thus be greater in regions where aseismic ridges subduct, but why is deformation associated with these stresses focused near the volcanic arc? In Kamchatka [*Wang*, 1996; *Kulinich et al*., 2007], Sumatra [*Sieh and Natawidjaja*, 2000], and Nicaragua [*Turner et al*., 2007], the partitioning of oblique convergence onto strike-slip faults coincident with the arc may reflect the higher heat-fluxes and mechanical weakening of the lithosphere. We suggest thermal weakening may also result in compressional deformation being focused here, resulting in uplift and broadening of the volcanic arc. This hypothesis is consistent with higher earthquake densities and the presence of shallow ($<$25 km) thrust earthquakes in the overthrusting plate near the Ecuadorian volcanic arc (Figure 9b), and near the Cordillera de Talamanca in Costa Rica (Figure 10b). It is also consistent with force balance calculations relating the elevation of volcanic-arc/highlands to the horizontal push transmitted through the wedge, and hence the shear strength of the megathrust [*Smith*, 1981; *Lamb and Davis*, 2003; *Lamb*, 2006].

The inner fore arc separates regions of lower rigidity in the outer fore arc and near the volcanic arc, providing a stable and relatively strong environment for the formation of fore-arc basins, fore-arc sliver plates, and accumulation of the elastic stresses recovered in earthquakes.

8.3.2. Interpretation of Seamount Morphology and Distributions

The residual bathymetric anomalies we interpret as subducting seamounts are similar in wavelength, amplitude, and morphology to seamounts observed seaward of the trench axis. These observations are inconsistent with models where the primary mechanical effect of seamount subduction is to increase normal stress on the subduction interface [*Scholz and Small*, 1997]. High normal stresses are generated by the flexural rigidity of the fore arc and such resistance to upward flexure would quickly increase the wavelength and reduce the amplitude of the bathymetric anomaly observed, making any morphological consistency with unsubducted seamounts unlikely.

In Figure 4c, we show that residual bathymetric anomalies associated with the subducting Louisville Ridge seamount chain are correlated with a local reduction (V_P up to 1 km s^{-1}) in fore-arc wave speeds. In the Mariana fore arc, serpentinite mud volcanoes cluster above large residual bathymetric anomalies associated with

subducting seamounts (Figure 5b). Both observations support the model of *Wang and Bilek* [2011, 2014], in which the subduction of bathymetric relief is accommodated by elevated degrees of upper-plate fracturing.

The form and distribution (Figure 12a) of residual bathymetric anomalies are also considered to be inconsistent with mechanical models proposing wholesale decapitation of subducting seamounts [*Cloos*, 1992; *Scholz and Small*, 1997]. The Mariana trench, for example, is located west of a portion of Pacific Plate characterized by a dense distribution of large (>2 km high) seamounts (Figure 5). Only 3–5, however, are presently interpreted beneath the fore arc. This density is consistent with the frequency with which seamounts will enter the trench over the next 5 Myr and a considerably higher density would be expected if a significant proportion were being accreted.

The ambiguity in identifying regions where seamounts are likely to have recently subducted drops considerably where linear seamount chains are identified. Few seamount chains are parallel with relative plate motion vectors, causing most collision zones to migrate with time. In Tonga, the rate of southward migration may be as high as 180 mm yr^{-1} [*Lonsdale*, 1986; *Ballance et al*., 1989], suggesting that the fore arc north and within 180 km of the contemporary collision zone may have been a site of seamount subduction within the last million years. This region is dashed in Figure 4a and bathymetric anomalies of similar amplitude to those observed in the contemporary collision zone are not observed. The region to the north may contain small fragments of broken up seamounts, but identification of isotopic and trace element signatures in arc lavas requiring up to ~40% of a slab-derived Louisville signature in arc volcanoes suggests the bulk of the Louisville Ridge is subducted [*Timm et al*., 2013].

In Japan, the collision zone between the Joban seamount chain and the Japan trench is migrating north, but large residual bathymetric anomalies are not observed south of the contemporary collision zone. This observation may be interpreted as suggesting seamounts are not accreted, or alternatively, that accreted seamounts lose all residual bathymetric expression. The later scenario is possible as seamounts lose their compensation, or are sufficiently fragmented that they lose their competence, but neither are preferred interpretations.

More generally, *Wessel et al*. [2010] used satellite-derived bathymetry to predict there may be as many 12,000 large seamounts with height, h, above the surrounding seafloor >1.5 km. *Hillier and Watts* [2007] used shipboard bathymetry data to predict there may be as many as 40,000 large ($h > 1$ km) seamounts, 60% of which remain to be discovered, and >200,000 probable seamounts of varying amplitude ($0.1 < h < 6.7$ km). Given these populations, if large-scale accretion were a process ubiquitous with seamount collision then the composition of both contemporary fore arcs and ancient subduction zones should be largely basaltic. Fragments of accreted seamounts in Japan are much smaller than the average dimensions of modern seamounts, which *Isozaki et al*. [1990] interpret as suggesting the bulk of colliding seamounts are subducted. The metamorphic grade of these fragments suggests deep lower crustal underplating of seamount material, as opposed to offscraping within an accretionary wedge, as the dominant mode of accretion with less than 1% of samples in the zeolite facies metamorphic grade. These observations are consistent with models where the majority of seamounts are subducted and while fractured seamounts may lose small pieces during subduction, as suggested by geochemical observations of rocks with OIB isotope and trace element signatures within fore arcs [*Geldmacher et al*., 2008], wholesale accretion is likely to be rare.

8.4. Influence on Seismicity

We have shown that regions of contemporary seamount subduction are typically associated with reduced levels of megathrust seismicity. Subduction of the Louisville ridge, for example, is associated with a 200 km wide gap in shallow (<65 km depth) seismicity, the width, and geometry of which suggest an association with the volcaniclastic filled flexural moat (Figure 4b) [*Bassett*, 2014]. Seamounts subducting beneath the central Mariana arc are similarly characterized by low-earthquake density and appear so against the more seismically active southern segment of the Mariana trench (Figure 5b). Tsunami earthquakes in Java were influenced by subducting relief, but rather than nucleating from or rupturing across a subducting seamount, the 2006 Mw 7.7 earthquake appears to have ruptured a comparatively smooth segment of the plate interface with eastward rupture propagation arrested by a subducting seamount (Figure 6c). A similar situation is observed in Japan and subduction of the Joban seamount chain is characterized by low-earthquake density, weak interseismic coupling, and may have limited southward rupture propagation

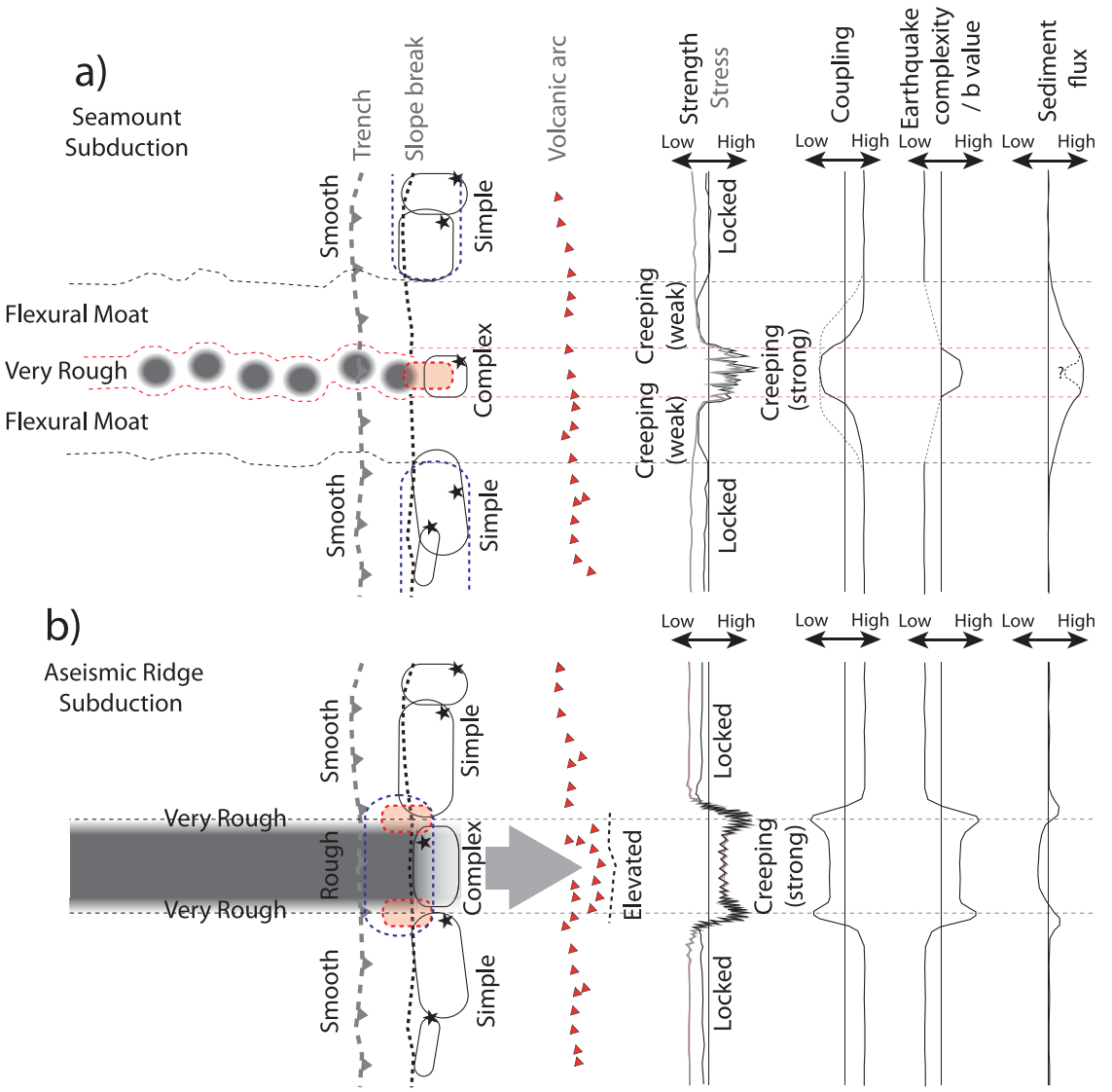

Figure 15. Cartoons summarizing the possible influence of subducting seamounts and aseismic ridges on structure and seismicity in subduction zones. Blue and filled red dash represents regions of moderate and high-earthquake density, respectively. Dotted black line marks the fore-arc slope break. (a) Subducting seamounts represent seafloor roughness over a narrow (typically <100 km) wavelength and fore-arc uplift and megathrust complexity are expected over a similar length-scale. The flexural compensation of seamounts may increase the flux of sediments, potentially reducing the strength of the megathrust and resulting in weak creeping zones either side of the seamount. (b) Aseismic ridges are locally compensated, resulting in a strong correlation between ridge physiography its influence on seismicity and plate-interface coupling. Megathrust complexity is greatest on the ridge flanks, explaining high densities of small earthquakes and rupture termination of large earthquakes. The megathrust may be less rough beneath the ridge crest, but remains sufficiently complex to facilitate strong creep and drive the additional deformation of the volcanic arc/highlands.

in the 2011 Mw 9.0 Tohoko-Oki earthquake (Figures 7b and 7c). The strength of conclusions that can be drawn from these observations is limited by the short duration of instrumental earthquake catalogs, but we do suggest that holistically, our observations of subducting relief are more consistent with associations with small earthquakes and creep than with large megathrust events. This translates into the question: how do bathymetric anomalies subduct aseismically?

The subducting seamounts interpreted above are ~1000–3000 km^2 in area, have residual bathymetric elevations ≥2 km and with respect to wavelength and amplitude, represent the end-member of subducting seafloor roughness (Figure 15a). At seismogenic depths, the "breaking through" model suggests that the geometrical incompatibility of this roughness may be accommodated by the development of an upper plate fracture network, the aseismic evolution of which is described by *Wang and Bilek* [2014]. They suggest that cataclasis and pressure solution are the dominant mechanisms facilitating aseismic creep.

Within the fracture network, the alternating failure of various parts of the system causes the network to deform almost continuously. Structural and stress heterogeneities limit the failure dimensions of individual fractures, resulting in large numbers of small magnitude earthquakes, as indicated by B-values where seamounts subduct offshore Costa Rica as large as ~2 [*Ghosh et al*., 2008]. Extrapolation of high B-values to low magnitudes implies a large number of brittle events below the resolution of seismometers and brecciation and comminution associated with the fracturing process leads to catalastic flow [*Wang and Bilek*, 2014]. Highly fractured rocks also allow a wide distribution of fluids, which may facilitate pressure solution creep occurring on the many block and grain boundaries within the fracture network.

The reduced levels of seismicity we observe may reflect the magnitude completeness of the earthquake catalogs we analyze with the numerous small earthquakes and microseismicity predicted by this model likely falling below the resolution (Mw≥3) of global earthquake catalogs [*Obana et al*., 2009; *Tréhu et al*., 2012]. Where large events are associated with subducting seamounts, these are likely, and have been shown, to be complex [*Bilek et al*., 2003; *Wang and Bilek*, 2011].

Subducting aseismic ridges or other large and laterally contiguous bathymetric features represent seafloor roughness over a larger scale than subducting seamounts, and the widths of ridges approach the rupture lengths of large (~Mw 7) megathrust earthquakes (Figure 15b). The steepest gradients, and hence the maximum seafloor and megathrust roughness, are associated with the ridge flanks and contrary to subducting seamounts, the lateral continuity of aseismic ridges means they do not have a steep frontal slope during subduction, except when they first collide with a margin. As a consequence, the plate interface across the central section of subducting ridges may be comparatively smooth and sufficiently wide that complex large earthquakes can rupture within this zone. The maximum roughness is associated with subducting ridge flanks, which may explain the high densities of small magnitude earthquakes and the tendency for earthquakes propagating from epicenters above the subducting ridge/plateau to stay within its bounds as is observed for earthquakes in Java (1994) and Costa-Rica (1941 and 1950). For earthquakes nucleating toward aseismic ridges, there are many examples of along-strike rupture propagation being arrested near the crest or flanks of these features [*Bilek*, 2010; *Sparkes et al*., 2010]. In South America, *Bilek* [2010] shows that the complexity and normalized source duration of moderate magnitude earthquakes (5.5> Mw >7.1) is greatest on the southern flanks of the subducting Nazca and Carnegie ridges, consistent with our suggestion of maximum roughness and complexity.

It thus seems likely that the mechanical processes by which oceanic seamounts, aseismic ridges, and oceanic plateau subduct are similar, with seafloor roughness promoting upper plate deformation and megathrust complexity enabling creep [*Wang and Bilek*, 2011, 2014]. In addition to where and the wavelength over which this roughness occurs (Figure 15), one additional and potentially important distinction between these features may be the mechanism of isostatic compensation [*Watts et al*., 2010]. Ridges and oceanic plateau are locally compensated because they formed on or near a mid-ocean ridge crest, which explains the close spatial correspondence between the residual bathymetric expression of these features and the extent of their influence on megathrust seismicity, geodetic locking (Dashed lines in Figures 9g and 15b) [*Chlieh et al*., 2011], and near arc physiography. Oceanic seamounts, in contrast, are often flexurally compensated providing local depressions where thick packets of volcaniclastic sediment may accumulate (Figure 15a). In Tonga, the width of the Louisville seismic gap is a factor >3 wider than the dimensions of seamounts entering the margin, which *Bassett* [2014] relate to the width of the flexural moat and the influence of higher sediment fluxes on the shear strength of the subduction interface (Figure 15a). The influence of subducting seamounts may thus extend beyond fracturing and deformation of the overthrusting plate, and what may be as important is their role in facilitating a larger flux of sediment into the seismogenic zone. This may occur either through subduction of a flexural moat [*Bassett*, 2014], or by altering the geometry of the megathrust [*Bell et al*., 2010].

9. Conclusions

An ensemble averaging technique is developed to isolate and remove the long-wavelength, large-amplitude (~7.5 km and ~200 mGal), trench-normal topography and gravity fields associated with subduction zones. This procedure lowers the dynamic range, removes the steep gradients associated with the seaward and landward trench-slopes and significantly increases the resolvability of short-wavelength/lower-

amplitude structure. Application of this technique to all subduction zones on Earth has resulted in the identification of >200 residual bathymetric anomalies within subduction fore arcs. Isolated anomalies with height ≥1 km and area ≥500 km^2 (N = 36), and aseismic ridges (N > 10), represent confident interpretations of subducting relief. Subducting fracture zones are resolved by residual free-air gravity anomalies up to >200 km landward of the trench-axis.

Isolated residual bathymetric anomalies interpreted as subducting seamounts are located near the trench (within 70 km), at shallow subducting slab depth (SLAB1.0 depth < 17 km) and are similar in wavelength, amplitude and morphology to unsubducted seamounts seaward of the trench-axis. The morphology and spatial distribution of subducting seamounts is not consistent with mechanical models proposing wholesale decapitation and accretion, and the majority of seamounts are likely subducted intact. Subducting seamounts are associated with reduced levels of megathrust seismicity and may have acted as barriers to rupture propagation in large earthquakes in Java and Japan.

Subducting aseismic ridges are associated with uplift and steepening of the outer-fore arc trench-slope, a gradual reduction in residual bathymetric expression across the inner fore arc, and a local increase in the width and elevation of the volcanic-arc/orogen. These contrasting expressions may reflect the influence of margin normal variations in rigidity on where and how the upper plate deforms, both to accommodate subducting relief and in response to stresses transmitted across the plate boundary. The outer-fore arc and near-arc regions may have lower rigidity due to fracturing and thermal weakening, respectively. Subducting aseismic ridges are associated with complex earthquakes and fault creep, and the, 'breaking through' model proposed to accommodate the geometrical incompatibility of subducting seamounts may also be applicable to the case of aseismic ridge subduction. This model proposes that bathymetric irregularities subduct by severely deforming and fracturing both the subducting anomaly and the overthrusting plate. The structural complexity and associated geometrical resistance against slip within this fracture network results in a strong megathrust and higher stress transmission across the subduction interface. Near-arc uplift landward of subducting ridges may reflect the predicted local increase in the magnitude of these stresses, which drive deformation that is focused near the arc due to the higher heat flux. Seafloor and megathrust roughness is greatest on the flanks of aseismic ridges, which explains the tendency for earthquakes propagating from epicenters within or away from regions of subducting aseismic ridges to terminate in these regions. The bathymetric expression of subducting ridges places strong constraints on the lateral extent over which subducting bathymetric anomalies influence the surface morphology of the fore arc trench-slope. Understanding the physical controls on these limits is an important subject worthy of future research.

Acknowledgments

We thank Laura Wallace, Heidrun *Kopp*, an anonymous reviewer and the editor Thorsten Becker for a helpful review. David Sandwell, Arnauld Heuret, Shamita Das, and Jason Phipps Morgan are thanked for helpful comments on an early version of this manuscript. David Sandwell is thanked further for providing an updated version (V23.1) of the global marine gravity grid. Cedric Twardzik and Johnny Hunter are thanked for helpful discussion. Figure construction and grid processing was conducted using GMT [*Wessel and Smith*, 1991, 1995, 1998]. This study is global in nature and the grids of residual free-air gravity anomaly and residual topography we generate are freely available as an electronic supplement and online. This study was supported in part by a University of Oxford Clarendon Scholarship and UK Natural Environment Research Council grants NE/F005318/1 and NE/1026839/1.

References

Abercrombie, R. E., M. Antolik, K. Felzer, and G. Ekström (2001), The 1994 Java tsunami earthquake: Slip over a subducting seamount, *J. Geophys. Res.*, *106*(B4), 6595–6607.

Ballance, P. F., D. W. Scholl, T. L. Vallier, and R. H. Herzer (1989), Subduction of a late Cretaceous seamount of the Louisville ridge at the Tonga trench: A model of normal and accelerated tectonic erosion *Tectonics*, *8*(5), 953–962.

Bangs, N. L., S. P. Gulick, and T. H. Shipley (2006), Seamount subduction erosion in the Nankai Trough and its potential impact on the seismogenic zone, *Geology*, *34*(8), 701–704.

Barckhausen, U., H. A. Roeser, and R. von Huene (1998), Magnetic signature of upper plate structures and subducting seamounts at the convergent margin off Costa Rica, *J. Geophys. Res.*, *103*(B4), 7079–7093.

Barker, D. H. N., R. Sutherland, S. Henrys, and S. Bannister (2009), Geometry of the Hikurangi subduction thrust and upper plate, North Island, New Zealand, *Geochem. Geophys. Geosyst.*, *10*, Q02007, doi:10.1029/2008GC002153.

Barrientos, S. E., and S. N. Ward (1990), The 1960 Chile earthquake: Inversion for slip distribution from surface deformation, *Geophys. J. Int.*, *103*(3), 589–598.

Bassett, D. (2014), The relationship between structure and seismogenic behaviour in subduction zones, unpublished PhD thesis, Dep. of Earth Sci., Univ. of Oxford, Oxford, U. K.

Bassett, D., and A. B. Watts (2015), Gravity anomalies, crustal structure, and seismicity at subduction zones: 2. Interrelationships between fore-arc structure and seismogenic behavior, *Geochem. Geophys. Geosyst.*, *16*, doi:10.1002/2014GC005685.

Bell, R., R. Sutherland, D. Barker, S. Henrys, S. Bannister, L. Wallace, and J. Beavan (2010), Seismic reflection character of the Hikurangi subduction interface, New Zealand, in the region of repeated Gisborne slow slip events, *Geophys. J. Int.*, *180*(1), 34–48.

Bilek, S. L. (2010), Invited review paper: Seismicity along the South American subduction zone: Review of large earthquakes, tsunamis, and subduction zone complexity, *Tectonophysics*, *495*(1), 2–14.

Bilek, S. L., and E. R. Engdahl (2007), Rupture characterization and aftershock relocations for the 1994 and 2006 tsunami earthquakes in the Java subduction zone, *Geophys. Res. Lett.*, *34*, L20311, doi:10.1029/2007GL031357.

Bilek, S. L., S. Y. Schwartz, and H. R. DeShon (2003), Control of seafloor roughness on earthquake rupture behavior, *Geology*, *31*(5), 455–458.

Billen, M. I., and M. Gurnis (2001), A low viscosity wedge in subduction zones, *Earth Planet. Sci. Lett.*, *193*(1), 227–236.

Billen, M. I., and M. Gurnis (2003), Comparison of dynamic flow models for the Central Aleutian and Tonga-Kermadec subduction zones, *Geochem. Geophys. Geosyst. 4*(4), 1035, doi:10.1029/2001GC000295.
Billen, M. I., M. Gurnis, and M. Simons (2003), Multiscale dynamics of the Tonga-Kermadec subduction zone, *Geophys. J. Int.*, *153*, 359–388.
Bird, P. (2003), An updated digital model of plate boundaries, *Geochem. Geophys. Geosyst. 4*(3), 1027,doi:10.1029/2001GC000252.
Bodine, J. H., and A. B. Watts (1979), On lithospheric flexure seaward of the Bonin and Mariana trenches, *Earth Planet. Sci. Lett.*, *43*, 132–148.
Bogdanov, N., and V. Khain (2000), Tectonic Map of the Sea of Okhotsk Region with Explanatory Notes, scale 1: 250,000, 171 pages, Inst. of the Lithosphere of Marginal Seas, Russ. Acad. of Sci., Moscow, Russ.
Bry, M., and N. White (2007), Reappraising elastic thickness variation at oceanic trenches, *J. Geophys. Res.*, *112*, B08414, doi:10.1029/2005JB004190.
Bürgmann, R., M. G. Kogan, G. M. Steblov, G. Hilley, V. E. Levin, and E. Apel (2005), Interseismic coupling and asperity distribution along the Kamchatka subduction zone, *J. Geophys. Res.*, *110*, B07405, doi:10.1029/2005JB003648.
Byrne, D. E., D. M. Davis, and L. R. Sykes (1988), Loci and maximum size of thrust earthquakes and the mechanics of the shallow region of subduction zones, *Tectonics*, *7*(4), 833–857.
Chlieh, M., H. Perfettini, H. Tavera, J. P. Avouac, D. Remy, J. M. Nocquet, F. Rolandone, F. Bondoux, G. Gabalda, and S. Bonvalot (2011), Interseismic coupling and seismic potential along the Central Andes subduction zone, *J. Geophys. Res.*, *116*, B12405, doi:10.1029/2010JB008166.
Cloos, M. (1992), Thrust-type subduction-zone earthquakes and seamount asperities: A physical model for seismic rupture, *Geology*, *20*(7), 601–604.
Cloos, M., and R. L. Shreve (1996), Shear-zone thickness and the seismicity of Chilean-and Marianas-type subduction zones, *Geology*, *24*(2), 107–110.
Clouard, V., and A. Bonneville (2005), Ages of seamounts, islands, and plateaus on the Pacific plate, *Spec. Pap. Geol. Soc. Am.*, *388*, 71.
Coffin, M. F., and O. Eldholm (1994), Large igneous provinces: Crustal structure, dimensions, and external consequences, *Rev. Geophys.*, *32*(1), 1–36.
Collot, J. Y., B. Marcaillou, F. Sage, F. Michaud, W. Agudelo, P. Charvis, D. Graindorge, M. A. Gutscher, and G. Spence (2004), Are rupture zone limits of great subduction earthquakes controlled by upper plate structures? Evidence from multichannel seismic reflection data acquired across the northern Ecuador-southwest Colombia margin, *J. Geophys. Res.*, *109*, B11103, doi:10.1029/2004JB003060.
Contreras-Reyes, E., I. Grevemeyer, A. B. Watts, L. Planert, E. R. Flueh, and C. Peirce (2010), Crustal intrusion beneath the Louisville hotspot track, *Earth Planet. Sci. Lett.*, *289*(3), 323–333.
Cottrell, R. D., and J. A. Tarduno (2003), A Late Cretaceous pole for the Pacific plate: Implications for apparent and true polar wander and the drift of hotspots, *Tectonophysics*, *362*(1–4), 321–333.
Dahlen, F. (1984), Noncohesive critical Coulomb wedges: An exact solution, *J. Geophys. Res.*, *89*(B12), 10,125–10,133.
Dahlen, F. (1990), Critical taper model of fold-and-thrust belts and accretionary wedges, *Annu. Rev. Earth Planet. Sci.*, *18*, 55.
Dahlen, F., J. Suppe, and D. Davis (1984), Mechanics of fold-and-thrust belts and accretionary wedges: Cohesive Coulomb theory, *J. Geophys. Res.*, *89*(B12), 10,087–10,101.
Das, S., and A. B. Watts (2009), Effect of subducting seafloor topography on the rupture characteristics of great subduction zone earthquakes, in *Subduction Zone Geodynamics*, edited by S. Lallemand and F. Funiciello, pp. 103–118, Springer.
Davies, G. F. (1981), Regional compensation of subducted lithosphere: Effects on geoid, gravity and topography from a preliminary model, *Earth Planet. Sci. Lett.*, *54*(3), 431–441.
Davis, D. M., J. Suppe, and F. A. Dahlen (1983), Mechanics of fold-and-thrust belts and accretionary wedges, *J. Geophys. Res.*, *88*(B2), 1153–1172.
Delouis, B., J. M. Nocquet, and M. Vallée (2010), Slip distribution of the February 27, 2010 Mw= 8.8 Maule earthquake, central Chile, from static and high-rate GPS, InSAR, and broadband teleseismic data, *Geophys. Res. Lett.*, *37*, L17305, doi:10.1029/2010GL043899.
DeMets, C., R. G. Gordon, and D. F. Argus (2010), Geologically current plate motions, *Geophys. J. Int.*, *181*(1), 1–80, doi:10.1111/j.1365-246X.2009.04491.x.
Dominguez, S., S. E. Lallemand, J. Malavieille, and R. von Huene (1998), Upper plate deformation associated with seamount subduction, *Tectonophysics*, *293*(3), 207–224.
Dominguez, S., J. Malavieille, and S. E. Lallemand (2000), Deformation of accretionary wedges in response to seamount subduction: Insights from sandbox experiments, *Tectonics*, *19*(1), 182–196.
Duncan, R. A., and R. A. Keller (2004), Radiometric ages for basement rocks from the Emperor Seamounts, ODP Leg 197, *Geochem. Geophys. Geosyst. 5*, Q08L03, doi:10.1029/2004GC000704.
Dziewonski, A., T. A. Chou, and J. Woodhouse (1981), Determination of earthquake source parameters from waveform data for studies of global and regional seismicity, *J. Geophys. Res.*, *86*(B4), 2825–2852.
Ekström, G., M. Nettles, and A. Dziewoński (2012), The global CMT project 2004–2010: Centroid-moment tensors for 13,017 earthquakes, *Phys. Earth Planet. Inter.*, *200*, 1–9. [Available at http://www.globalcmt.org/CMTsearch.html, last accessed Jan. 2015.]
Emerman, S. H., and D. Turcotte (1983), A fluid model for the shape of accretionary wedges, *Earth Planet. Sci. Lett.*, *63*(3), 379–384.
Engdahl, E. R., R. van der Hilst, and R. Buland (1998), Global teleseismic earthquake relocation with improved travel times and procedures for depth determination, *Bull. Seismol. Soc. Am.*, *88*(3), 722–743. [Available at http://www.isc.ac.uk/ehbbulletin/, last accessed Jan. 2015.]
England, P., R. Engdahl, and W. Thatcher (2004), Systematic variation in the depths of slabs beneath arc volcanoes, *Geophys. J. Int.*, *156*(2), 377–408.
Fox, P. J., E. Schreiber, H. Rowlett, and K. McCamy (1976), The geology of the oceanographer fracture zone: A model for fracture zones, *J. Geophys. Res.*, *81*(23), 4117–4128.
Fryer, P. (2012), Serpentinite mud volcanism: Observations, processes, and implications, *Annu. Rev. Mar. Sci.*, *4*, 345–373.
Fryer, P., and G. J. Fryer (1987), Origins of nonvolcanic seamounts in a forearc environment, in *Seamounts, Islands, and Atolls*, edited by B. H. Keating, P. Fryer, R. Batiza, and G. W. Boehlert, pp. 61–69, AGU, Washington, D. C.
Fryer, P., and N. C. Smoot (1985), Processes of seamount subduction in the Mariana and Izu-Bonin trenches, *Mar. Geol.*, *64*(1), 77–90.
Fryer, P., E. Ambos, and D. Hussong (1985), Origin and emplacement of Mariana forearc seamounts, *Geology*, *13*(11), 774–777.
Fryer, P., C. Wheat, and M. Mottl (1999), Mariana blueschist mud volcanism: Implications for conditions within the subduction zone, *Geology*, *27*(2), 103–106.
Fujie, G., S. Miura, S. Kodaira, Y. Kaneda, M. Shinohara, K. Mochizuki, T. Kanazawa, Y. Murai, R. Hino, and T. Sato (2013), Along-trench structural variation and seismic coupling in the northern Japan subduction zone, *Earth Planets Space*, *65*, 75–83.
Gao, X., and K. Wang (2014), Strength of stick-slip and creeping subduction megathrusts from heat flow observations, *Science*, *345*(6200), 1038–1041.

Geldmacher, J., K. Hoernle, P. Van Den Bogaard, F. Hauff, and A. Klügel (2008), Age and geochemistry of the Central American forearc basement (DSDP Leg 67 and 84): Insights into Mesozoic arc volcanism and seamount accretion on the fringe of the Caribbean LIP, *J. Petrol.*, *49*(10), 1781–1815.

Ghosh, A., A. V. Newman, A. M. Thomas, and G. T. Farmer (2008), Interface locking along the subduction megathrust from b-value mapping near Nicoya Peninsula, Costa Rica, *Geophys. Res. Lett.*, *35*, L01301, doi:10.1029/2007GL031617.

Graindorge, D., A. Calahorrano, P. Charvis, J. Y. Collot, and N. Bethoux (2004), Deep structures of the Ecuador convergent margin and the Carnegie Ridge, possible consequence on great earthquakes recurrence interval, *Geophys. Res. Lett.*, *31*, L04603, doi:10.1029/2003GL018803.

Grevemeyer, I., and E. Flueh (2008), TOTAL: TOnga Thrust earthquake Asperity at Louisville Ridge, *FS Sonne Fahrtbericht/Cruise Rep. SO 195*, IFM-GEOMAR, Kiel, Germany.

Habermann, R., W. McCann, and B. Perin (1986), Spatial seismicity variations along convergent plate boundaries, *Geophys. J. R. Astron. Soc.*, *85*(1), 43–68.

Hager, B. H. (1984), Subducted slabs and the geoid: Constraints on mantle rheology and flow, *J. Geophys. Res.*, *89*(B7), 6003–6015.

Hanks, T. C. (1971), The Kuril trench-Hokkaido rise system: Large shallow earthquakes and simple models of deformation, *Geophys. J. Int.*, *23*(2), 173–189.

Hastings, D. A., and P. Dunbar (1998), Development and assessment of the global land one-km base elevation digital elevation model (GLOBE), *Group*, *4*(6), 218–221.

Hatherton, T. (1969), Similarity of gravity anomaly patterns in asymmetric active regions, *Nature, 224*, 357–358.

Hayes, D. E. (1966), A geophysical investigation of the Peru-Chile trench, *Mar. Geol.*, *4*(5), 309–351.

Hayes, D. E., and M. Ewing (1970), Pacific boundary structure, in *The Sea, 4*(part II), pp. 27–72, Wiley, N. Y.

Hayes, D. E., and M. Ewing (1971), Louisville Ridge. A possible extension of the Eltanin Fraction Zone, *AGU Antarct. Res. Ser.*, *15*, 223–228.

Hayes, G. P., D. J. Wald, and R. L. Johnson (2012), Slab1. 0: A three-dimensional model of global subduction zone geometries, *J. Geophys. Res.*, *117*, B01302, doi:10.1029/2011JB008524.

Heuret, A., C. Conrad, F. Funiciello, S. Lallemand, and L. Sandri (2012), Relation between subduction megathrust earthquakes, trench sediment thickness and upper plate strain, *Geophys. Res. Lett.*, *39*, L05304, doi:10.1029/2011GL050712.

Heuret, A., S. Lallemand, F. Funiciello, C. Piromallo, and C. Faccenna (2011), Physical characteristics of subduction interface type seismogenic zones revisited, *Geochem. Geophys. Geosyst. 12*, Q01004, doi:10.1029/2010GC003230.

Hillier, J. K., and A. B. Watts (2007), Global distribution of seamounts from ship-track bathymetry data, *Geophys. Res. Lett.*, *34*, L13304, doi:[10.1029/2007GL029874.

Hunter, J. A., A. B. Watts, and D. Bassett (2013), Flexural modelling of gravity anomalies seaward of Pacific subduction zones, Abstract EGU2013–9847 presented at EGU 10th General Assembly, Vienna.

Hussong, D. (1982), Structure and tectonics of the mariana arc and fore-arc-drill-site selection surveys, *Init. Rep. Deep Sea Drill. Proj.*, *60*, 33–44.

Hussong, D., and S. Uyeda (1982), Tectonic processes and the history of the Mariana arc-a synthesis of the results of deep-sea drilling Project Leg-60, *Init. Rep. Deep Sea Drill. Proj.*, *60*, 909–929.

Ide, S., A. Baltay, and G. C. Beroza (2011), Shallow dynamic overshoot and energetic deep rupture in the 2011 Mw 9.0 Tohoku-Oki earthquake, *Science*, *332*(6036), 1426–1429.

Intergovernmental Oceanographic Commission (IOC) (2003), BODC, 2003, Centenary Edition of the GEBCO Digital Atlas [CD-ROM], published on CD-ROM on behalf of the Intergovernmental Oceanographic Commission and the International Hydrographic Organization as part of the General Bathymetric Chart of the Oceans, Brit. Oceanogr. Data Cent., Liverpool.

Isozaki, Y., S. Maruyama, and F. Furuoka (1990), Accreted oceanic materials in Japan, *Tectonophysics*, *181*(1), 179–205.

Johnson, J. M., and K. Satake (1999), Asperity distribution of the 1952 great Kamchatka earthquake and its relation to future earthquake potential in Kamchatka, in *Seismogenic and Tsunamigenic Processes in Shallow Subduction Zones*, pp. 541–553, Springer.

Kanamori, H., and M. Kikuchi (1993), The 1992 Nicaragua earthquake: A slow tsunami earthquake associated with subducted sediments, *Nature*, *361*(6414), 714–716.

Kelleher, J. (1972), Rupture zones of large South American earthquakes and some predictions, *J. Geophys. Res.*, *77*(11), 2087–2103.

Kelleher, J., and W. McCann (1976), Buoyant zones, great earthquakes, and unstable boundaries of subduction, *J. Geophys. Res.*, *81*(26), 4885–4896.

Kelleher, J., L. Sykes, and J. Oliver (1973), Possible criteria for predicting earthquake locations and their application to major plate boundaries of the Pacific and the Caribbean, *J. Geophys. Res.*, *78*(14), 2547–2585.

Kelleher, J., J. Savino, H. Rowlett, and W. McCann (1974), Why and where great thrust earthquakes occur along island arcs, *J. Geophys. Res.*, *79*(32), 4889–4899.

Keller, R. A., M. R. Fisk, and W. M. White (2000), Isotopic evidence for Late Cretaceous plume-ridge interaction at the Hawaiian hotspot, *Nature*, *405*(6787), 673–676.

Kodaira, S., N. Takahashi, A. Nakanishi, S. Miura, and Y. Kaneda (2000), Subducted seamount imaged in the rupture zone of the 1946 Nankaido earthquake, *Science*, *289*(5476), 104–106.

Kodaira, S., E. Kurashimo, J.-O. Park, N. Takahashi, A. Nakanishi, S. Miura, T. Iwasaki, N. Hirata, K. Ito, and Y. Kaneda (2002), Structural factors controlling the rupture process of a megathrust earthquake at the Nankai trough seismogenic zone, *Geophys. J. Int.*, *149*(3), 815–835.

Koketsu, K., Y. Yokota, N. Nishimura, Y. Yagi, S. i. Miyazaki, K. Satake, Y. Fujii, H. Miyake, S. i. Sakai, and Y. Yamanaka (2011), A unified source model for the 2011 Tohoku earthquake, *Earth Planet. Sci. Lett.*, *310*(3), 480–487.

Kopp, H. (2013), Invited review paper: The control of subduction zone structural complexity and geometry on margin segmentation and seismicity, *Tectonophysics*, *589*, 1–16.

Kopp, H., D. Klaeschen, E. R. Flueh, J. Bialas, and C. Reichert (2002), Crustal structure of the Java margin from seismic wide-angle and multichannel reflection data, *J. Geophys. Res.*, *107*(B2), ETG 1–1-ETG 1–24.

Koppers, A. A. P., R. A. Duncan, and B. Steinberger (2004), Implications of a nonlinear 40Ar/39Ar age progression along the Louisville seamount trail for models of fixed and moving hot spots, *Geochem. Geophys. Geosyst. 5*, Q06L02, doi:10.1029/2003GC000671.

Koppers, A. A. P., et al. (2012), Limited latitudinal mantle plume motion for the Louisville hotspot, *Nat. Geosci.*, *5*(12), 911–917.

Kulinich, R., B. Y. Karp, B. Baranov, E. Lelikov, V. Karnaukh, M. Valitov, S. Nikolaev, T. Kolpashchnikova, and I. Tsoi (2007), Structural and geological characteristics of a "seismic gap" in the central part of the Kuril Island Arc, *Russ. J. Pacific Geol.*, *1*(1), 3–14.

Kumagai, H., N. Pulido, E. Fukuyama, and S. Aoi (2012), Strong localized asperity of the 2011 Tohoku-Oki earthquake, Japan, *Earth Planets Space*, *64*(7), 649–654.

Lallemand, S., and X. Le Pichon (1987), Coulomb wedge model applied to the subduction of seamounts in the Japan Trench, *Geology*, *15*(11), 1065–1069.
Lallemand, S., R. Culotta, and R. von Huene (1989), Subduction of the Daiichi Kashima seamount in the Japan trench, *Tectonophysics*, *160*(1), 231–247.
Lamb, S. (2006), Shear stresses on megathrusts: Implications for mountain building behind subduction zones, *J. Geophys. Res.*, *111*, B07401, doi:10.1029/2005JB003916.
Lamb, S., and P. Davis (2003), Cenozoic climate change as a possible cause for the rise of the Andes, *Nature*, *425*(6960), 792–797.
Lay, T., C. J. Ammon, H. Kanamori, L. Xue, and M. J. Kim (2011), Possible large near-trench slip during the 2011 M (w) 9. 0 off the Pacific coast of Tohoku Earthquake, *Earth Planets Space*, *63*(7), 687–692.
Levin, V., J. Park, M. Brandon, J. Lees, V. Peyton, E. Gordeev, and A. Ozerov (2002), Crust and upper mantle of Kamchatka from teleseismic receiver functions, *Tectonophysics*, *358*(1), 233–265.
Levitt, D. A., and D. T. Sandwell (1995), Lithospheric bending at subduction zones based on depth soundings and satellite gravity, *J. Geophys. Res.*, *100*(B1), 379–400.
Lonsdale, P. F. (1986), A multibeam reconnaissance of the Tonga Trench axis and its intersection with the Louisville guyot chain, *Mar. Geophys. Res.*, *8*(4), 295–327.
Loveless, J. P., and B. J. Meade (2010), Geodetic imaging of plate motions, slip rates, and partitioning of deformation in Japan, *J. Geophys. Res.*, *115*, B02410, doi:10.1029/2008JB006248.
Loveless, J. P., and B. J. Meade (2011), Spatial correlation of interseismic coupling and coseismic rupture extent of the 2011 MW= 9.0 Tohoku-oki earthquake, *Geophys. Res. Lett.*, *38*, L17306, doi:10.1029/2011GL048561.
Masson, D., L. Parson, J. Milsom, G. Nichols, N. Sikumbang, B. Dwiyanto, and H. Kallagher (1990), Subduction of seamounts at the Java Trench: A view with long-range sidescan sonar, *Tectonophysics*, *185*(1), 51–65.
Matthews, K. J., R. D. Müller, P. Wessel, and J. M. Whittaker (2011), The tectonic fabric of the ocean basins, *J. Geophys. Res.*, *116*, B12109, doi: 10.1029/2011JB008413.
McAdoo, D., J. Caldwell, and D. Turcotte (1978), On the elastic-perfectly plastic bending of the lithosphere under generalized loading with application to the Kuril Trench, *Geophys. J. Int.*, *54*(1), 11–26.
Mochizuki, K., T. Yamada, M. Shinohara, Y. Yamanaka, and T. Kanazawa (2008), Weak interplate coupling by seamounts and repeating M∼ 7 earthquakes, *Science*, *321*(5893), 1194–1197.
Morgan, E., B. McAdoo, and L. Baise (2008), Quantifying geomorphology associated with large subduction zone earthquakes, *Basin Res.*, *20*(4), 531–542.
Nishizawa, A., K. Kaneda, N. Watanabe, and M. Oikawa (2009), Seismic structure of the subducting seamounts on the trench axis: Erimo Seamount and Daiichi-Kashima Seamount, northern and southern ends of the Japan Trench, *Earth Planets Space*, *61*(3), e5–e8.
Oakley, A., B. Taylor, and G. Moore (2008), Pacific Plate subduction beneath the central Mariana and Izu-Bonin fore arcs: New insights from an old margin, *Geochem. Geophys. Geosyst. 9*, Q06003, doi:10.1029/2007GC001820.
Obana, K., S. Kodaira, and Y. Kaneda (2009), Seismicity at the eastern end of the 1944 Tonankai earthquake rupture area, *Bull. Seismol. Soc. Am.*, *99*(1), 110–122.
Parsons, B., and P. Molnar (1976), The origin of outer topographic rises associated with trenches, *Geophys. J. Int. 1*(4), 707–712.
Pavlis, N. K., S. A. Holmes, S. C. Kenyon, and J. K. Factor (2012), The development and evaluation of the Earth Gravitational Model 2008 (EGM2008), *J. Geophys. Res.*, *117*, B04406, doi:10.1029/2011JB008916.
Peirce, C., and A. B. Watts (2011), The Louisville Ridge: Tonga Trench collision: Implications for subduction zone dynamics, *R/V Sonne SO215, Cruise Rep.*, Dep. of Earth Sci., Durham Univ., Durham.
Planert, L., H. Kopp, E. Lueschen, C. Mueller, E. Flueh, A. Shulgin, Y. Djajadihardja, and A. Krabbenhöft (2010), Lower plate structure and upper plate deformational segmentation at the Sunda-Banda arc transition, Indonesia, *J. Geophys. Res.*, *115*,.
Pontoise, B., B. Pelletier, J. Aubouin, N. Baudry, R. Blanchet, J. Butscher, P. Chotin, M. Diament, J. Dupont, and J. Eissen (1986), Subduction of Louisville ridge along the Tonga Trench-preliminary-results of Seapso Campaign (LEG-V), *C. R. Acad. Sci. Ser. II*, *303*(10), 911–918.
Prince, R. A., and D. W. Forsyth (1988), Horizontal extent of anomalously thin crust near the Vema fracture zone from the three-dimensional analysis of gravity anomalies, *J. Geophys. Res.*, *93*(B7), 8051–8063.
Protti, M., K. McNally, J. Pacheco, V. González, C. Montero, J. Segura, J. Brenes, V. Barboza, E. Malavassi, and F. Güendel (1995), The March 25, 1990 (Mw= 7.0, ML= 6.8), earthquake at the entrance of the Nicoya Gulf, Costa Rica: Its prior activity, foreshocks, aftershocks, and triggered seismicity, *J. Geophys. Res.*, *100*(B10), 20,345–20,358.
Ranero, C. R., and R. von Huene (2000), Subduction erosion along the Middle America convergent margin, *Nature*, *404*(6779), 748–752.
Robb, J. M., and M. F. Kane (1975), Structure of the Vema fracture zone from gravity and magnetic intensity profiles, *J. Geophys. Res.*, *80*(32), 4441–4445.
Robinson, D., and L. Cheung (2010), Source process of the Mw 8.3, 2003 Tokachi-Oki, Japan earthquake and its aftershocks, *Geophys. J. Int.*, *181*(1), 334–342.
Robinson, D. P., S. Das, and A. B. Watts (2006), Earthquake rupture stalled by a subducting fracture zone, *Science*, *312*(5777), 1203–1205.
Ruff, L. J. (1989), Do trench sediments affect great earthquake occurrence in subduction zones?, in *Subduction Zones Part II*, pp. 263–282, Springer.
Sallarès, V., and C. R. Ranero (2005), Structure and tectonics of the erosional convergent margin off Antofagasta, north Chile (23 30′ S), *J. Geophys. Res.*, *110*, B06101, doi:10.1029/2004JB003418.
Sandwell, D. T., and W. H. F. Smith (1997), Marine gravity anomaly from Geosat and ERS 1 satellite altimetry, *J. Geophys. Res.*, *102*, 10,039–10,054.
Sandwell, D. T., and W. H. F. Smith (2009), Global marine gravity from retracked Geosat and ERS-1 altimetry: Ridge segmentation versus spreading rate, *J. Geophys. Res.*, *114*, B01411, doi:10.1029/2008JB006008.
Sandwell, D. T., D. T. Muüller, W. H. F. Smith, E. Garcia, and R. Francis (2014), New global marine gravity from CryoSat-2 and Jacon-1 reveals buried tectonic structure, *Science*, *346*(6205), 65–67.
Schöffel, H. J., and S. Das (1999), Fine details of the Wadati-Benioff zone under Indonesia and its geodynamic implications, *J. Geophys. Res.*, *104*(B6), 13,101–13,114.
Scholl, D. W., S. Kirby, and R. von Huene (2011), Exploring a link between great and giant megathrust earthquakes and relative thickness of sediment and eroded debris in the subduction channel to roughness of subducted relief, Abstracts T14B-01 presented at 2011 Fall Meeting, AGU, San Francisco, Calif.
Scholz, C. H., and C. Small (1997), The effect of seamount subduction on seismic coupling, *Geology*, *25*(6), 487–490.

Shulgin, A., H. Kopp, C. Mueller, L. Planert, E. Lueschen, E. Flueh, and Y. Djajadihardja (2011), Structural architecture of oceanic plateau subduction offshore Eastern Java and the potential implications for geohazards, *Geophys. J. Int.*, *184*(1), 12–28.
Sieh, K., and D. Natawidjaja (2000), Neotectonics of the Sumatran fault, Indonesia, *J. Geophys. Res.*, *105*(B12), 28,295–28,326.
Simkin, T., and L. Siebert (2002), Volcanoes of the world: An illustrated catalog of holocene volcanoes and their eruptions, *Global Volcanism Prog. Digital Inf. Ser., GVP-3*, Smithsonian Inst.
Simons, M., S. E. Minson, A. Sladen, F. Ortega, J. Jiang, S. E. Owen, L. Meng, J.-P. Ampuero, S. Wei, and R. Chu (2011), The 2011 magnitude 9.0 Tohoku-Oki earthquake: Mosaicking the megathrust from seconds to centuries, *Science*, *332*(6036), 1421–1425.
Singh, S. C., N. Hananto, M. Mukti, D. P. Robinson, S. Das, A. Chauhan, H. Carton, B. Gratacos, S. Midnet, and Y. Djajadihardja (2011), Aseismic zone and earthquake segmentation associated with a deep subducted seamount in Sumatra, *Nat. Geosci.*, *4*(5), 308–311.
Smith, A. G. (1981), Subduction and coeval thrust belts, with particular reference to North America, *Geol. Soc. London Spec. Publ.*, *9*(1), 111–124.
Smith, W. H. F., and D. T. Sandwell (1997), Global sea floor topography from satellite altimetry and ship depth soundings, *Science*, *277*, 1956–1962.
Song, T., and M. Simons (2003), Large trench-parallel gravity variations predict seismogenic behavior in subduction zones, *Science*, *301*(5633), 630–633.
Sparkes, R., F. Tilmann, N. Hovius, and J. Hillier (2010), Subducted seafloor relief stops rupture in South American great earthquakes: Implications for rupture behaviour in the 2010 Maule, Chile earthquake, *Earth Planet. Sci. Lett.*, *298*(1), 89–94.
Spence, W. (1977), The Aleutian arc: Tectonic blocks, episodic subduction, strain diffusion, and magma generation, *J. Geophys. Res.*, *82*(2), 213–230.
Spence, W., C. Mendoza, E. Engdahl, G. Choy, and E. Norabuena (1999), Seismic subduction of the Nazca Ridge as shown by the 1996–97 Peru earthquakes, in *Seismogenic and Tsunamigenic Processes in Shallow Subduction Zones*, edited by J. Sauber, R. Dmowska, pp. 753–776, Birkhauser Verlag, Basel.
Stratford, W., C. Peirce, M. Funnell, M. Paulatto, A. B. Watts, I. Grevemeyer, and D. Bassett (2015), Effect of Seamount subduction on forearc morphology and seismic structure of the Tonga-Kermadec subduction zone, *Geophys. J. Int.*, *200*, 1503–1522, doi:10.1093/gji/ggu475.
Swenson, J. L., and S. L. Beck (1996), Historical 1942 Ecuador and 1942 Peru subduction earthquakes and earthquake cycles along Colombia-Ecuador and Peru subduction segments, *Pure Appl. Geophys.*, *146*(1), 67–101.
Sykes, L. R. (1971), Aftershock zones of great earthquakes, seismicity gaps, and earthquake prediction for Alaska and the Aleutians, *J. Geophys. Res.*, *76*(32), 8021–8041.
Syracuse, E. M., and G. A. Abers (2006), Global compilation of variations in slab depth beneath arc volcanoes and implications, *Geochem. Geophys. Geosyst. 7*, Q05017, doi:10.1029/2005GC001045.
Tajima, F., and M. Kikuchi (1995), Tectonic implications of the seismic ruptures associated with the 1983 and 1991 Costa Rica earthquakes, *Geol. Soc. Am. Spec. Pap.*, *295*, 327–340.
Takahashi, N., S. Kodaira, S. L. Klemperer, Y. Tatsumi, Y. Kaneda, and K. Suyehiro (2007), Crustal structure and evolution of the Mariana intra-oceanic island arc, *Geology*, *35*(3), 203–206.
Talwani, M., G. H. Sutton, and J. L. Worzel (1959), A crustal section across the Puerto Rico trench, *J. Geophys. Res.*, *64*(10), 1545–1555.
Talwani, M., J. L. Worzel, and M. Ewing (1961), Gravity anomalies and crustal section across the Tonga Trench, *J. Geophys. Res.*, *66*(4), 1265–1278.
Tarduno, J. A., et al. (2003), The Emperor Seamounts; southward motion of the Hawaiian Hotspot plume in Earth's mantle, *Science*, *301*(5636), 1064–1069.[10.1126/science.1086442][Not Given in Reference][25278606]
Taylor, F. W., R. W. Briggs, C. Frohlich, A. Brown, M. Hornbach, A. K. Papabatu, A. J. Meltzner, and D. Billy (2008), Rupture across arc segment and plate boundaries in the 1 April 2007 Solomons earthquake, *Nat. Geosci.*, *1*(4), 253–257.
Timm, C., D. Bassett, I. J. Graham, M. I. Leybourne, C. de Ronde, J. Woodhead, D. Layton-Matthews, and A. B. Watts (2013), Louisville seamount subduction and its implication on mantle flow beneath the central Tonga-Kermadec arc, *Nat. Commun.*, *4*, 1–8.
Tréhu, A. M., R. J. Blakely, and M. C. Williams (2012), Subducted seamounts and recent earthquakes beneath the central Cascadia forearc, *Geology*, *40*(2), 103–106.
Turner, H. L., P. LaFemina, A. Saballos, G. S. Mattioli, P. E. Jansma, and T. Dixon (2007), Kinematics of the Nicaraguan forearc from GPS geodesy, *Geophys. Res. Lett.*, *34*, L02302, doi:10.1029/2006GL027586.
Uyeda, S., and H. Kanamori (1979), Back-arc opening and the mode of subduction, *J. Geophys. Res.*, *84*(B3), 1049–1061.
Vannucchi, P., D. M. Fisher, S. Bier, and T. W. Gardner (2006), From seamount accretion to tectonic erosion: Formation of Osa Mélange and the effects of Cocos Ridge subduction in southern Costa Rica, *Tectonics*, *25*, TC2004, doi:10.1029/2005TC001855.
Vening-Meinesz, F. A., P. H. Kuenen, and J. Umbrove (1932), *Gravity Expeditions at Sea*, Waltman.
von Huene, R., C. Ranero, W. Weinrebe, and K. Hinz (2000), Quaternary convergent margin tectonics of Costa Rica, segmentation of the Cocos Plate, and Central American volcanism, *Tectonics*, *19*(2), 314–334.
Wallace, L. M., Å. Fagereng, and S. Ellis (2012), Upper plate tectonic stress state may influence interseismic coupling on subduction megathrusts, *Geology*, *40*(10), 895–898.
Walther, C. H. (2003), The crustal structure of the Cocos ridge off Costa Rica, *J. Geophys. Res.*, *108*(B3), 2136, doi:10.1029/2001JB000888.
Wang, K. (1996), Simplified analysis of horizontal stresses in a buttressed forearc sliver at an oblique subduction zone, *Geophys. Res. Lett.*, *23*(16), 2021–2024.
Wang, K., and S. L. Bilek (2011), Do subducting seamounts generate or stop large earthquakes?, *Geology*, *39*(9), 819–822.
Wang, K., and S. L. Bilek (2014), Invited review paper: Fault creep caused by subduction of rough seafloor relief, *Tectonophysics*, *610*, 1–24.
Wang, K., and Y. Hu (2006), Accretionary prisms in subduction earthquake cycles: The theory of dynamic Coulomb wedge, *J. Geophys. Res.*, *111*, B06410, doi:10.1029/2005JB004094.
Watts, A. B., and M. Talwani (1974), Gravity anomalies seaward of deep-sea trenches and their tectonic implications, *Geophys. J. Int.*, *36*(1), 57–90.
Watts, A. B., and M. Talwani (1975), Gravity effect of downgoing lithospheric slabs beneath island arcs, *Geol. Soc. Am. Bull.*, *86*(1), 1–4.
Watts, A. B., J. K. Weissel, R. A. Duncan, and R. L. Larson (1988), Origin of the Louisville ridge and its relationship to the Eltanin fracture zone system, *J. Geophys. Res.*, *93*(B4), 3051–3077.
Watts, A. B., A. A. P. Koppers, and D. P. Robinson (2010), Seamount subduction and earthquakes, *Oceanography*, *23*(1), 166–173.
Wells, R. E., R. J. Blakely, Y. Sugiyama, D. W. Scholl, and P. A. Dinterman (2003), Basin-centered asperities in great subduction zone earthquakes: A link between slip, subsidence, and subduction erosion?, *J. Geophys. Res.*, *108*(B10), 2507, doi:10.1029/2002JB002072.
Wessel, P., and W. H. Smith (1991), Free software helps map and display data, *Eos Trans. AGU*, *72*(41), 441–446.
Wessel, P., and W. H. Smith (1995), New version of the generic mapping tools released, *EOS Trans. AGU*, *76*, 329.

Wessel, P., and W. H. Smith (1998), New, improved version of generic mapping tools released, *Eos Trans. AGU*, *79*(47), 579–579.
Wessel, P., D. T. Sandwell, and S.-S. Kim (2010), The global seamount census, *Oceanography*, *23*(1), 24–33.
Worzel, J. L. (1965), *Pendulum Gravity Measurements at Sea, 1936-59*, p. 1, Wiley, N. Y.
Zhao, D., Z. Huang, N. Umino, A. Hasegawa, and H. Kanamori (2011), Structural heterogeneity in the megathrust zone and mechanism of the 2011 Tohoku-oki earthquake (Mw 9.0), *Geophys. Res. Lett.*, *38*, L17308, doi:10.1029/2011GL048408.
Zhong, S., and M. Gurnis (1992), Viscous flow model of a subduction zone with a faulted lithosphere: Long and short wavelength topography, gravity and geoid, *Geophys. Res. Lett.*, *19*(18), 1891–1894.
Zhong, S., and M. Gurnis (1994), Controls on trench topography from dynamic models of subducted slabs, *J. Geophys. Res.*, *99*(B8), 15,683–15,695.
Zhong, S., M. Gurnis, and L. Moresi (1998), Role of faults, nonlinear rheology, and viscosity structure in generating plates from instantaneous mantle flow models, *J. Geophys. Res.*, *103*(B7), 15,255–15,268.